KERNFORSCHUNGSANLAGE JÜLICH
GESELLSCHAFT MIT BESCHRÄNKTER HAFTUNG
Institut für Reaktorwerkstoffe

Quality Control Procedures on Graphite, Pyrocarbon and Siliconcarbide

Papers presented at the 8th meeting of the Dragon Project Quality Control Working Party, AEE Winfrith, England, 11th and 12th of June, 1974

compiled by

K. Koizlik

Jül - 1106 - RW
September 1974

Als Manuskript gedruckt

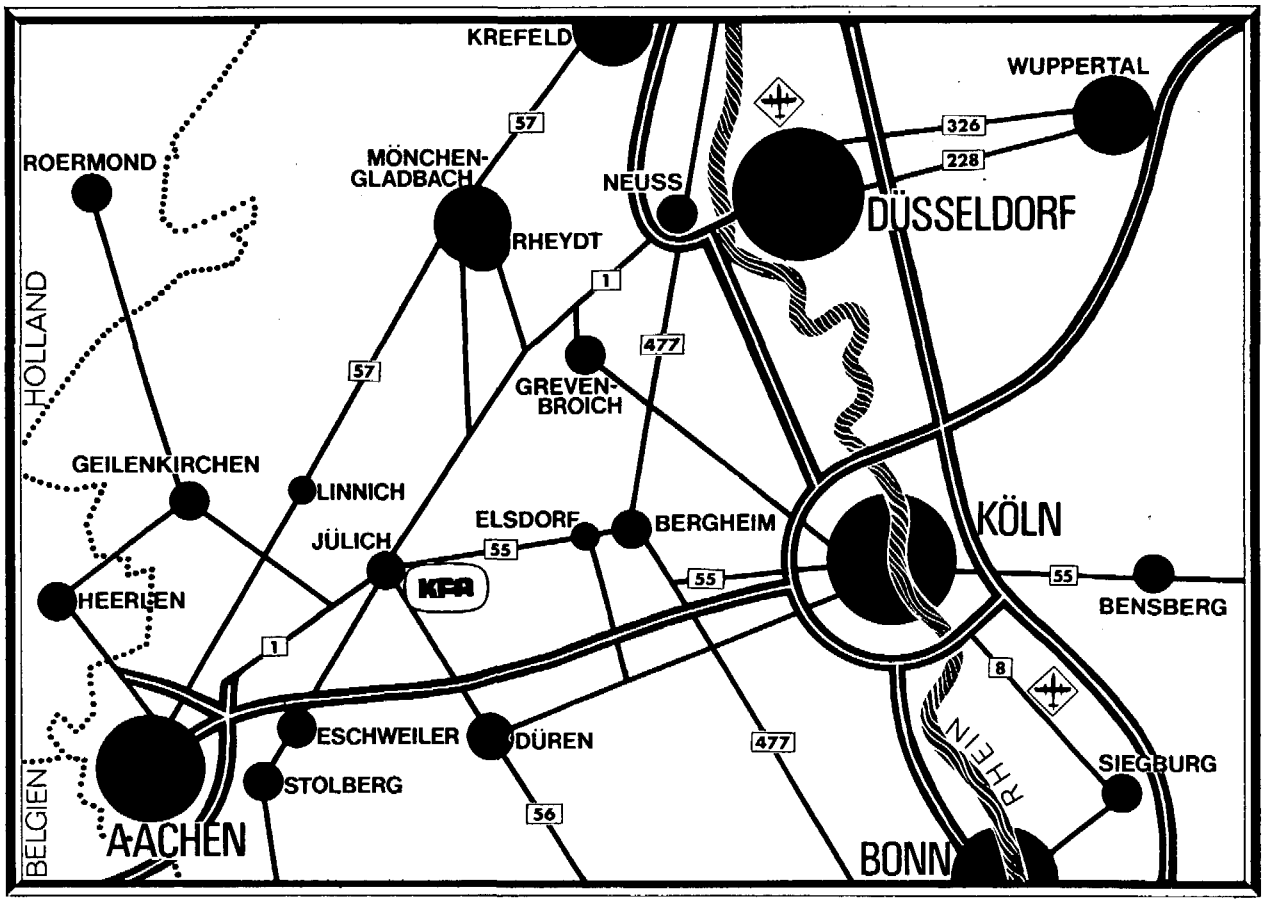

Berichte der Kernforschungsanlage Jülich – Nr. 1106
Institut für Reaktorwerkstoffe Jül - 1106 - RW

Dok.: HTR Fuels
Graphite
Silicon Carbides
Pyrolytic Carbon
Quality Control Procedures
Structural Analysis

Im Tausch zu beziehen durch: ZENTRALBIBLIOTHEK der Kernforschungsanlage Jülich GmbH, Jülich, Bundesrepublik Deutschland

Quality Control Procedures on Graphite, Pyrocarbon and Siliconcarbide

Papers presented at the 8th meeting of the Dragon Project Quality Control Working Party, AEE Winfrith, England, 11th and 12th of June, 1974

compiled by

K. Koizlik

Work reported here has been done by

Mrs. S. Allen	OECD Dragon Project, Winfrith / England
R. Blackstone	RCN Petten, Holland / The Netherlands
Fr. M. Cremerius	Kernforschungsanlage Jülich
W. W. Delle	"
M. R. Everett	OECD Dragon Project, Winfrith / England
P. D. Frampton	"
J. Holliday	"
J. C. Hedderly	"
H. Hoven	Kernforschungsanlage Jülich
K. Koizlik	"
P. Krautwasser	"
H. Luhleich	"
H. Schuster	"
K. Täuber	"
E. Wallura	"
C. Yust	ORNL, Oak Ridge, Tennessee / USA

QUALITY CONTROL PROCEDURES ON GRAPHITE, PYROCARBON AND SILICONCARBIDE

Papers presented at the 8th meeting
of the Dragon Project Quality Control Working Party,
AEE Winfrith, England, 11th and 12th of June, 1974

compiled by

K. Koizlik

ABSTRACT

The presented report includes those papers presented at the 8th meeting of the DP-QCWP in Winfrith which have been written by collaborators of the Institut für Reaktorwerkstoffe der Kernforschungsanlage Jülich, together with other co-authors. The papers deal with problems of standardizing characterization methods for the routine quality control of graphites and pyrolytic carbons as well as with more basic procedures (transmission electron microscopy, microporosity) for the analysis of pyrocarbon structure.

Kernforschungs-
anlage Jülich
GmbH IRW

JÜL - 1106 - RW

September 1974

VERFAHREN ZUR QUALITÄTSKONTROLLE BEI GRAPHIT, PYROKOHLENSTOFF UND SILIZIUMKARBID

Beiträge zum achten Treffen der
Dragon Project Quality Control Working Party,
AEE Winfrith, England, 11. und 12. Juni 1974

Zusammengestellt von

K. Koizlik

KURZFASSUNG

Der vorliegende Bericht enthält diejenigen Beiträge zum achten Treffen der DP QCWP in Winfrith, die von Mitarbeitern des Instituts für Reaktorwerkstoffe der Kernforschungsanlage Jülich zusammen mit anderen Koautoren geschrieben wurden. Diese Beiträge behandeln Probleme der Standardisierung von Charakterisierungsverfahren für die routinemäßige Qualitätskontrolle von Graphiten und Pyrokohlenstoffen. Daneben werden auch Untersuchungsverfahren wie Transmissionselektronenmikroskopie oder Röntgenkleinwinkelstreuung für die Mikroporositätsmessung beschrieben, die der Strukturaufklärung von Pyrokohlenstoff dienen.

Contents

1. Introduction

Graphite and pyrocarbon are used for different purposes in High Temperature Gas Cooled Reactors (HTGR). To date pyrocarbon is exclusively used as coating material of the fuel kernels to prevent the fission products from being released into the cooling gas. Graphite, on the other hand, and **graphitic** materials have a wide field of application in HTGR technology.
Because of the different microstructures, production procedures and functions in an HTGR, the graphites, graphitic materials and pyrocarbons have to be specified and characterized. Since these materials are technological products, they have to be controlled during production with respect to their properties and the specifications. The necessary requirement of a sufficient quality control gave rise to the introduction of a system of characterization procedures, which should supply the producers as well as the reactor operating institutions with the informations about the material.
During the first stages of the mentioned work only very few characterization procedures were available, and by this the knowledge about the material was very poor. It should be mentioned, indeed, that because of the better knowledge of the process of production and the as large as necessary samples from the beginning graphite and graphitic materials were better known than pyrocarbon. The intensive work during the last years on the field of characterization has brought a lot of informations about these materials, on the one hand, but has shown, on the other hand, that a so called "complete set" of material parameters for the prediction of its behaviour in a reactor is up today not yet at hand. So two very important questions arose:

a) Which of the large number of material parameters in graphite and pyrocarbon are necessary and sufficient to describe and - as far as possible - to predict the irradiation behaviour of these materials and to control the production process. These parameters are often called "key parameters". So the question has to be answered: Which properties can act as key parameters?

b) The more the information about graphite and pyrocarbon structure and properties increased, the more decreased the impartiality to the correct and adequate definition of the various material parameters. For almost each of the measured properties several often quite different definitions and measuring procedures are available, thus giving rise to a considerable insecurity in characterizing materials. To overcome this insecurity is the second important task for the next future.

The presented report and the lectures printed in it as well as the Dragon Project Quality Control Working Party as a whole have to be seen on the background of these two problems. This report is part of a series of publications to describe results of investigations done by KFA alone or together with other institutiones to contribute to the answers of the mentioned questiones.

2. Methods of Evaluation for Graphite

Discussion of availability of standard methods for testing graphites to be used in HTGR

by

W.W. Delle

M.R. Everett

R. Blackstone

Introduction:

Since many years graphite has been manufactured for conventionel applications in a large scale. The necessary quality control has been experienced by the manufactures. Physical and chemical methods for the characterization have been developed to meet the requirements of the customers. As far as standards were available they could be applied in the quality control laboratories. Sometimes characterization methods had to be taken from other materials showing certain aspects of the graphite behaviour. When graphite became more and more important as power reactor components the question of validity of the available standard measuring methods became important.

As a first step the standard methods used in the United States (ASTM) and in the Federal Republic of Germany (DIN) were investigated due to their validity for reactor components. Furthemore both standards were compared as far as possible. Details of the investigation can be taken from tables 1 to 6.

From previous discussions resulted that the key parameters for the evaluation of a graphite may be:*

- Nuclear purity
- Apparent density
- Thermal conductivity
- Thermal expansion
- Young's modulus of elasticity
- Strength
- Isotropy
- Degree of graphitization
- Defects

The present investigation shows that sufficient standard methods are available for apparent density, strength, thermal expansion (partially) and impurities (partially) only as far as the ASTM standard is concerned. The DIN standard is often not applicable for graphite. In the moment the question, if the test specimens irradiated in MTRs meet the requirements of the standards, is open.

---

* M.R. Everett, R. Blackstone, R. Krefeld:
DPTN/560 (QCWP/P75), April 1974

Table 1-1 US (ASTM) and German (DIN) Standards for Particular Graphite Properties

Property	ASTM Standard	Comments	DIN Standard	Comments
Bulk Density	C-559-69	Density in air of manufactured carbon and graphite articles	51065	Density in air (and water displacement) of ceramic raw and semifinished materials, bulk density of bricks and fragments
Thermal Expansion	E 227-71	Standard method of test for linear thermal expansion of rigid solids with vitreous silica dilatometer	52328	Testing of glass; determination of linear expansion coefficient
Thermal Conductivity	C-714-72	Standard method of test for thermal diffusivity of carbon and graphite by a thermal pulse method	52612 52613	Disk method Tube method
Flexural Strength	C-651-70	Standard method of test for flexural strength of manufactured carbon and graphite articles using four-point loading at room temperature	51223 53452	Description of machines for flexural strength investigations. Relevant for molded articles and compounds
Tension testing (Tensile strength)	C-565-71	Testing of carbon-graphite mechanical materials	51221	Description of tensile testing machines, general requirements- Not specific for graphite or ceramic materials
Young's Modulus	not available		not available	
Poisson's Ratio	not available		not available	

Table 1-2 US (ASTM) and German (DIN) Standards for Particular Graphite Properties

Property	ASTM Standard	Comments	DIN Standard	Comments
Compressive Strength (Crushing Str.)	C-695-71 T	Tentative Method of Test for compressive (crushing) strength of graphite	51223	Description of machiens for compressive strength investigations. No information about specimens to be used.
Impact Strength	not available		53453	Standard for investigations of plastics
Ash	C-561-69	Determination of the ash content of graphite	51719	Determination of ashes in fossil fuel
Moisture	C-562-69	Determination of the percentage of moisture in graphite	not available	
Chemical Analysis	C-560-69	Analysis of Silicon, Iron, Calcium, Aluminium, Titanium, Vanadium, Boron no informations about Barium, Copper, Nickel, Strontium	not available	

Table 2-1 Comparison of Standard Methods for Bulk Density

	ASTM C-559-69	DIN 51065
Scope	Determination of density from measurements of weight an dimensions in air at 25°C. Applicable to boronated carbon or graphite, a dispersion of boron in either carbon or graphite shapes, used for control rods and neutron shielding in nuclear technology.	Determination of density in air from measurements of weight and dimensions at room temperature. Determination also by use of displacement of water or mercury.
Defination	Density: the weight in air of a unit volume including both permeable and impermeable voids (and boron compounds in the case of boronated carbon or boronated graphite), present in the material at 25°C.	Ratio of mass to volume of matter including pores density = $\frac{\text{mass}}{\text{volume}}$
Test Specimens	Form of a right circular cylinder or rectangular parallelepiped with no dimension smaller than five times the length of the largest visible particle. Volume shall not be less than 0,5 cm^3. Specimen is to be dried for a min. of 2 h at 110°C and then to be cooled to 25 ± 5°C in a desiccator	Specimens have to be cleaned before investigation. Three specimens must be measured. Specimens are to be dried at 110 ± 2°C and then to be cooled to room temperature in a desiccator. Volume about 100 cm^3 (if test does not require smaller or bigger specimens).
Procedure	Measurements to an accuracy of 0,05%. Sufficient number of measurements to determine the mean of each dimension. Weight of the test specimen in grams to a precision of 0.05%.	Measurements of specimens up to 100 g to an accuracy 0.01%. Above 100 g to an precision of 0.1%. Volume: Specimens saturated with water are measured in water and air by the use of a hydrostatic balance. The difference of both weighings in g corresponds to the volume of the specimen in cm^3.
Calculations	Density = $\frac{W_g}{V_{cm^3}}$ W_g = weight, g in air, V_{cm^3} = volume, cm^3 Density is to be calculated to four significant figures.	

Table 2 - 2 Comparison of Standard Methods for Bulk Density

	ASTM C-559-69	DIN 51065
Report	The report shall include the type, source, grade, and form of the sample and the densities of the individual specimens and the average	The report shall include kind of material, shape of specimen, impreguation method, procedure of volume determination. Apparent densities of the individual specimens and the average in g/cm^3 with an accuracy of 0.01 g/cm^3, date of investigation.
Note		DIN 51065 also describes mercury density.

Table 3-1 Comparison of standard methods for the Coefficient of Linear Thermal Expansion (CTE)

	ASTM E 228-71	DIN 52328
Scope	Determination of CTE by a vitreous silica dilatometer from - 195 to + 1.000°C for rigid solids including metals, ceramics and refractories, glasses, rocks and minerals, plastics, wood, and inorganic cements, pastes, and mortars .	Determination of Mean Coefficient of Linear Thermal Expansion of glass in a limited temperature range in the elastic-brittle state below the transformation region.
Definitions	1. Linear Thermal Expansion is the change in length per unit length resulting from a change in temperature of the material. Symbolically represented by $\Delta L/L_o$, where ΔL ist the observed change in length and L_o is the length of the specimen at reference temperature T_o, linear thermal expansion has the units of inches per inch, or centimeters per centimeter, often expressed as percentage or parts per million. 2. Mean Coefficient of Linear Thermal Expansion, α_m, between temperatures T_1 and T_2, is defined as: $\alpha_m = (L_2 - L_1)/L_o(T_2 - T_1) = \Delta L/(L_o \cdot \Delta T)$ where L_1 and L_2 = specimen lengths at temperatures T_1 and T_2, respectively. α_m is therefore obtained by dividing the linear thermal expansion ($\Delta L/L_o$) by the change of temperature (ΔT) . Units are inches per inch, or centimeter per centimeter per degree change in temperature, often expressed in parts per million per degree. 3. Instantaneous Coefficient of Linear Thermal Expansion , α_T, at temperature T, is defined by the following expression: $\alpha_T = \lim_{T_1 \to T_2} (L_2 - L_1)/L_o(T_2 - T_1) = dL/(dT \cdot L_o)$ α_T has the same units as α_m .	Coefficient of Linear Thermal Expansion, α, of a material ist the ratio of fractional length change to temperature change by which the length change is caused $\alpha = \frac{1}{L_o} \cdot \frac{\Delta L}{\Delta T}$ L_o = length of specimen ΔL = length change of spec. ΔT = temperature difference.

Table 3 - 2 Comparison of standard methods for the Coefficient of Linear Thermal Expansion (CTE)

	ASTM E 228-71	DIN 52328
Apparatus	1. Dilatometer of the tube or rod type, fabricated of high-purity vitreous silica. Typical dilatometers of these two types are schown in Figs.1-1 and 1-2 2. Extensometer, for measuring length changes over a length of at least 0.050 in. (1.27 mm). The graduated scale shall permit direct reading to 0.0001 in. 0.003 mm) and estimates of 0.00002 in. (0.0005 mm). Its accuracy shall be such that the error of indication will not exceed ± 0.00005 in. (0.0013 mm) for any length change. 3. Micrometer Calipers, with an index permitting direct reading of 0.001 in. (0.025 mm) for measuring the initial specimen length. A high-grade screw micrometer customarily used in machine shop practice is satisfactory. 4. Electric Furnace, capable of maintaining the difference between the maximum and minimum temperatures of the specimen within 2 C. The details of typical furnaces are shown in Figs.1-3 and 1-4 Temperature-control equipment shall maintain the mean temperature of the specimen within ±2 C of the desired test temperature. 5. Liquid Baths may be used when expansion data below 100 C are required. The bath shall be arranged so that a uniform temperature throughout the specimen is maintained. Means to control the desired temperature to within ± 0.2 C shall be provided.	Dilatometer for measuring the length change with an accuracy of 0.00002 . L_o Device for measuring L_o with an accuracy of 0.1% . Furnace with a temperature constance over the specimen length of ± 3°C.

Table 3 - 3 Comparison of standard methods for the Coefficient of Linear Thermal Expansion (CTE)

	ASTM E 228-71	DIN 52328
Apparatus	6. Temperature-Measuring Instruments - A calibrated thermocouple shall be provided for determining the temperature of the test specimen. Type T, E, S, K, or J thermocouples may be used. Types T and E can be calibrated to indicate temperatures accurate to ± 0.2 C and ± 0.5 C, respectively in the range - 190 to 350 C. A Type S thermocouple can be calibrated to indicate temperatures accurate to ± 0.5 C in the range 0 to 1000 C and is especially recommended for use in the range 350 to 1000 C. A Type S thermocouple should not be used for subzero temperatures. A Type K thermocouple can be calibrated to indicate temperatures accurat to ± 0.5 C in the range - 190 to 350 C. A Type J thermocouple can be calibrated to indicate temperatures accurate to ± 0.5 C in the range 0 to 350 C. The thermocouple shall be referenced to 0 C by means of an icewater bath or its equivalent ice-point reference system and its emf measured with a calibrated potentiometer having a sensitivity of ± 1 µV and an accuracy of ± 5 µV. Precautions shall be taken to ensure that the reference junction is maintained at 0 C throughout the test.	Temperature-Measuring Instruments (for example thermocouples) which allow to measure the temperature of the specimen and of the temperature difference, Δt, with an accuracy of ± 2°C

Table 3 - 4 Comparison of standard methods for the Coefficient of Linear Thermal Expansion (CTE)

	ASTM E 228-71	DIN 52328
Test Specimens	Specimen length should be between 2 and 5 in. (51 and 127 mm). Generally, specimens shorter than 2 in. result in a loss of sensitivity while specimens longer than 5 in. are subject to axial temperature differences in excess of the specified 2 C because of furnace gradients. The minimum diameter or thickness of the specimen shall be 1/16 in. (4.8 mm) or 1/16 of the specimen length, whichever is smaller. The maximum diameter or thickness is determined by the inside diameter of the tube-type dilatometer and the distance between fixed and transmission rods in the rod-type dilatometer. The shapes of specimen ends and the vitreous silica contact surface shall be designed so that the specimen remains laterally fixed during the test. Figure 1-5 illustrates some commonly accepted designs	Specimen length shall be at least 5×10^4 times as long as is the inaccuracy of the length change measurement.
Procedures	Detailled informations are given for the specimen treatments as well as for series of constant temperatures, heating or cooling at constant rate.	Before measuring, the specimens shall be heated up to remove inner stresses (informations for glass only). The measuring length of the specimen is measured at room temperature with an accuracy of $\pm$ 0.001 L All temperatures and temperature differences have to be determined with an accuracy of $\pm$ 2 degree.

Table 3 - 5 Comparison of standard methods for the Coefficient of Linear Thermal Expansion (CTE)

	ASTM E 228-71	DIN 52328
Calculations	Linear thermal expansion: $\Delta L/L_o = \left[(\Delta L)_\alpha / L_o\right] + \left[(\Delta L)_s / L_o\right]$ where: L_o = length of the test specimen at the reference temperature T_o. $(\Delta L)_\alpha$ = apparent changes in speciment length from the test temperature T_1 to the test temperature T_2, and $(\Delta L)_s / L_o$ = change in length per unit length of vitreous silica from T_1 to T_2 Mean coefficient of linear thermal expansion: $\alpha_m = \Delta L/L_o \Delta T = \left[(\Delta L)_\alpha / L_o \Delta T\right] + \left[(\Delta L)_s / L_o \Delta T\right]$ where ΔT = temperature difference between the test temperatures T_1 and T_2. Instantaneous coefficient of linear thermal expansion at any temperature, T: $\alpha_T = (dL/dT)/L_o$ where dL/dT = slope of the length-versus-temperature curve at temperature T. The slope may be determined by either graphical or mathematical analysis.	$\alpha = \frac{L}{L_o} \times \frac{\Delta L}{\Delta T}$ where: L_o = length of specimen ΔL = length change of spec. ΔT = temperature difference If a differential dilatometer is used the following formula is valid $\alpha = \frac{L}{L_o} \times \frac{\Delta L}{\Delta T} + \alpha_Q$ where: α_Q = mean coefficient of thermal expansion of the device for the transmission of measured values for the temperature region.

Table 3 - 6 Comparison of standard methods for the Coefficient of Linear Thermal Expansion (CTE)

	ASTM E 228-71	DIN 52328
Report	The report shall include - Description of material, including name of manufacturer, chemical composition, thermal and mechanical history. - Method of preparation of test specimen, axis orientation if material is anisotropic, and thermal, mechanical, moisture, or other conditioning. - Form and dimensions of test specimen, including initial length L_o, and reference temperature T_o, - Brief description of the apparatus, including displacement and temperature measuring systems, estimate of precision, heating and cooling rates, and temperature controls.	The report shall include - Description of material including manufacturer - Specimen shape, length and number of specimens - Type of dilatometer

Table 4-1 Comparison of Standard Methods for Thermal Conductivity

	ASTM C 714-72	DIN 52613
Scope	Determination of the thermal diffusivity of carbons and graphite to ± 5 percent at temperatures up to 500 C. It requires only a small easily fabricated specimen. Thermal diffusivity values in the range from 0.04 to 2.0 cm^2/s are readily measurable by this method.	Determination of thermal conductivity by the tube method. Thermal conductivity shall not be higher than abut 0.003 cal/cm sec ^{o}C. Measuring temperature up to 1.000 ^{o}C.
Apparatus and Method	A high-intensity short-duration thermal pulse from a flash lamp ist absorbed on the front surface of a specimen and the rear surface temperature-change as a function of time is observed on an oscilloscope. The pulse raises the average temperature of the specimen only a few degrees above its initial value. The ambient temperature of the specimen is controlled by a furnace or cryostat. Thermal diffusivity is calculated from the specimen thickness and the time required for the temperature of the back surface to rise to one half of its maximum value. The essential features of the apparatus are shown in Fig.	The measuring system consists of two coaxial metallic tubes with a core heater held in the centre of the inner tube and with the specimen contained in the annulus between the inner and outer metallic tube.
Test Specimens	The specimen shall be a circular disk. 2 to 4 mm thick and 6 to 12 mm in diameter, however, several things must be considered in choosing specimen dimensions. The diameter is fairly arbitrary except that it must not be too large relative to the flash source because the front surface of the specimen must be illuminated uniformly and, therefore, heated uniformly.	The specimen has to be dried at 105 ^{o}C at atmospheric pressure. It must be in good contact with the coaxial tube. No air space is allowed.

Table 4 - 2 Comparison of Standard Methods for Thermal Conductivity

	ASTM C 714-72	DIN 52613
Calculation	Thermal diffusivity: $\alpha = wL^2 / t_{1/2}$ where: L = thickness of the specimen, cm, $t_{1/2}$ = time for the rear surface temperature to rise to one half of its maximum value, s, and w = parameter that is a function of the heat loss Where heat losses from the sample are significant or where the duration of the thermal pulse is not sufficiently short, techniques for the necessary corrections must be applied. Note: From thermal diffusivity thermal conductivity must be using the equation: $K = \alpha\, dc$ where: α = thermal diffusivity d = density c = specific heat at constant pressure.	$K = \frac{F}{2\pi} \frac{\ln(da/di)}{L(T_1 - T_2)}$ where: di = inner diameter da = outer diameter of the specimen L = length of measuring T_1 = mean temperature at the inner surface T_2 = mean temperature at the outer surface of the specimen
Report	The report shall include thermal pulse source, method of calculation, identification and previous history of the test specimen, calculated value of thermal diffusivity, and density of the specimen.	The report shall include laboratory, date of measurement, customer, material, kind of specimen selection, measures of specimens, pre- treatment and apparent density of the specimens, mean temperature difference, $T_1 - T_2$, with an accuracy to 0.1°C, measuring temperature to 1°C.

Table 5-1 Comparison of Standard Methods for Flexural Strength

	ASTM 651-70	DIN 53452 / 53223
Scope	Determination of the flexural strength of manufactured carbon and graphite articles using a simple beam in four-point loading at room temperature	Determination of strength of moulded articles using different velocities of deformation and temperatures
Definition	Flexual strength - a measure of the ultimate load-carrying capacity of a specified beam in bending.	Flexural strength is the ratio of the moment of flexure to moment of resistance.
Apparatus	The four-point loading ficture shall consist of bearing blocks which ensure that forces applied to the beam are normal only and without eccentricity. The bearing block diameter shall be between 1/10 and 1/20 of the specimen support span. A hardened steel bearing block or its equivalent is necessary to prevent distortion of the loading member. The directions of loads and reactions may be maintained parallel by judicious use of linkages, rocker bearings, and flexure plates. Eccentricity of loading can be avoided by the use of spherical bearings. Provision must be made in fixture design for relief of torsional loading to less than 5 percent of the nominal specimen strength . Refer to the attached figure for a suggested four-point loading fixture, (Fig. 3-3)	The apparatus is described in the special standard DIN 51227 which is concerned with various machines for mechanical investigations

Table 5 - 2 Comparison of Standard Methods for Flexural Strength

	ASTM 651-70	DIN 53452 / 53223
Test Specimens	Preparation - The test specimen shall be prepared to yield a parallelepiped of rectangular cross section. The faces shall be parallel and flat within 0.001 in. (0.025 mm)/in. of length. In addition, the samples having a maximum particle size less than 0.006 in. (o.152 mm) diameter must be finished so that the surface roughness is less than 125 µin. AA. Sample edges should be free from visible flaws and chips. Size - The size of the test specimen shall be selec t ed such that the minimum dimension of the specimen is greater than 5 times the largest particle dimen s- ion. The test specimen shall have a length to thickness ratio of at least 8, and a width to thickness ratio of at least 2. Measurements - All dimensions shall be measured to the nearest 0.5 percent. Orientation - The specimen shall be marked on the end to denote its orientation with respect to the parent stock. Drying - Each specimen must be dried in an oven at 11o C for a period of 2 h. The sample must then be cooled to room temperature in a desiccator and held there prior to testing.	The specimen shape depends upon the kind of material. The surface must be free from scratches. All mechanical treatments shall be made in the direction parallel to the axis of the specimen. Size of the specimen: 1. Length, L = 120 ± 2 mm width, b = 15 ± 0,5 mm height, h = 10 ± 0,5 mm (or outer diameter, D) 2. Length, L = 50 ± 1 mm width, b = 6 ± 0,2 mm height, h = 4 ± 0,2 mm (or outer diameter, D) 3. Rods: $L \geq 10 \times D$

Table 5 - 3 Comparison of Standard Methods for Flexural Strength

	ASTM 651-70	DIN 53452 / 53223
Procedure	The load is centered applying bearing surfaces and the test specimen on the bearing blocks. The load span is at least two times the sample thickness, and the support span three times the load span, but not less than 1 1/2 in. (38.1 mm). Each end of the specimen is overlapped by at least the specimen thickness. The load applying bearing surfaces shall make contact with the upper surface of the test specimen. Load and support bearing blocks must be parallel to each other and perpendicular to the test surfaces. A loading rate of 0.05 in. (1.27 mm) /min or less on screw-driven testing machines is used. Measurements to 0.001 in. (0.025 mm) shall be made to determine the average width and thickness of the specimen at the section of failure. The load at failure must be recorded to an accuracy of $\pm$ 2 percent of the fullscale value. A full-scale value of 1000 lb (454 kg) would require recording to an accuracy of $\pm$ 20 lb ($\pm$ 9.08 kg).	The specimens have to be kept at $20 \pm 2^{\circ}C$ for at least 16 h at a relative atmospheric moisture of 65 ± 5 %. The specimen is used as a beam supported on both ends. The load is applied in the middle between both supports (Fig.3-1) Before investigation the cross section is measured to an accuracy of 0.01 mm^2. The experiment shall be carried out at $20^{\circ}C$. During deformation no shock shall be applied on the specimen. The feed velocity shall be adjusted in a way that the experiment can be finished after 1 min
Calculations	If the fracture occurs within the span length between the load bearing surfaces, calculate the flexural strength as follows: $S = PL/bd^2$ where: S = flexural strength, psi (kgf/mm^2) P = maximum applied load indicated by the testing machine, lb (kg), L = support span length, in. (mm). b = average width of specimen, in. (mm), and d = average thickness of specimen, in. (mm),	Ultimate flexural strength is $S = \frac{M}{W}$ in kp/cm^2 where: M = moment of flexure in kp cm W = moment of resistance in cm^2 $M = \frac{P \cdot L_s}{4}$ P = maximum applied load in kp L_s = support span length in cm

Table 5 - 4 Comparison of Standard Methods for Flexural Strength

	ASTM 651-70	DIN 53452 / 53223
Calculations	If the fracture occurs outside of the span length between load bearing blocks, the results of the test shall be discarded but reported. If fracture occurs in less than 5 s, the results shall be discarded but reported. A multiplying factor of 703.07 may be used to convert psi to kgf/m^2.	For rectangular cross-section: $W = \frac{b \cdot h^4}{6}$ b = width of specimen in cm, h = height of specimen in cm For a round rod: $W \approx 0.1\ D^3$ D = Outer diameter in cm, d = Inner diameter in cm For a tube: $W \approx \frac{D^4 - d^4}{D}$
Report	The report of each test shall include sample identification, average width to the nearest 0.001 in. (0.025 mm), average thickness to the nearest 0.001 in. (0.025 mm), span length, in. (mm), rate of loading (in./mm or ppm), Maximum applied load, lb (kg), flexural strength calculated to the nearest 10 psi (0.7 kgf/cm^2), defects in specimen, orientation and location of specimen, and failure mode and location.	The report shall include kind and identification of material. Date of production, shape and measures of the specimen, condition of specimen, machining, location of the specimen in the block, kind and duration of pre-treatment, measuring temperature, moisture in air. Flexural strength in kp/cm^2 to the nearest 5 kp/cm^2 Bending at fracture to the nearest 0.1 mm.

Table 6-1 Comparison of Standard Methods for the Determination of Ash in Graphite

	ASTM C 561-69	DIN 51719
Scope	Determination of the ash content of graphite	Determination of the ash content of fossil fuel to get informations about the portion of anorganic constituents
Definition		Ash is the expression for the remaining substance after combustion at $(775^{\circ} \pm 25)^{\circ}C$
Apparatus	Platinum dish, 100 ml capacity Analytical balance, capable of weighing to 0.0002 g Muffle furnace, capable of reaching 950°C. Controller for furnace, capable of maintaining $950 \pm 20^{\circ}C$ Platinum wire, 4 - in. (102-mm)length Desiccator charged with indicating desiccant.	Porcelain dish, round shaped of 40 mm outer diameter or quadrangular 40 mm x 50 mm, 10 mm rim. Muffle furnace heated electrically or by gas, to be controlled automatically. Also necessary for the procedure after DIN-Standard but not mentioned under apparatus .
Test Specimens	The entire sample of graphite should be crushed and ground to pass a No.60 (250 µm) sieve in a roll crusher. The sample may have been reduced in size initially by drilling the test bar with silicone carbide-tipped drills.	Specimen of 1 g ± 50 mg is weighed to an accuracy of 0.001 g.
Procedure	Introduction of a slow stream of air into the cold muffle furnace. Heating up of furnace so that it reaches 500°C in 1 h and 750°C in 2 h. After the carbon has burned offs as shown by the absence of black flecks upon stirring the sample with a platinum wire increase of temperature of the furnace to 950°C for 1 h. Cooling in a desiccator and then weighing the dish and ask as rapidly as possible, following its removal from the desiccator. Replacing sample in 950°C furnace for 1/2 h and repetition of the procedure until a constant weight is obtained to ± 0.0002 g .	Placing of the specimen into the cold muffle furnace. The furnace is to be heated up slowly to $(775 \pm 25)^{\circ}C$ till the material is burnt off. This is the case if no black flecks can be found out by stirring the sample with a platinum wire or a spatula. After shut-down of the heating the specimen is left in the furnace for a short time the door being opened, then cooled down in a desiccator and weighed with an accuracy of 0.0001 g.

Table 6 - 2 Comparison of Standard Methods for the Determination of Ash in Graphite

	ASTM C 561-69	DIN 51719
Calculation	Ash, % = $\left[(C - A)/(B - A)\right]$ x 100 where: A = weight of dish, B = weight of dish and dried sample, and C = weight of dish and ash.	Ash, % = $\frac{b \cdot 100}{a}$ (ash content per 100 g weight) weight before heating = a g fuel weight after heating = b g ash
Report	The report shall include proper identification of the sample and results obtained from at least two ash determinations, and their averages.	

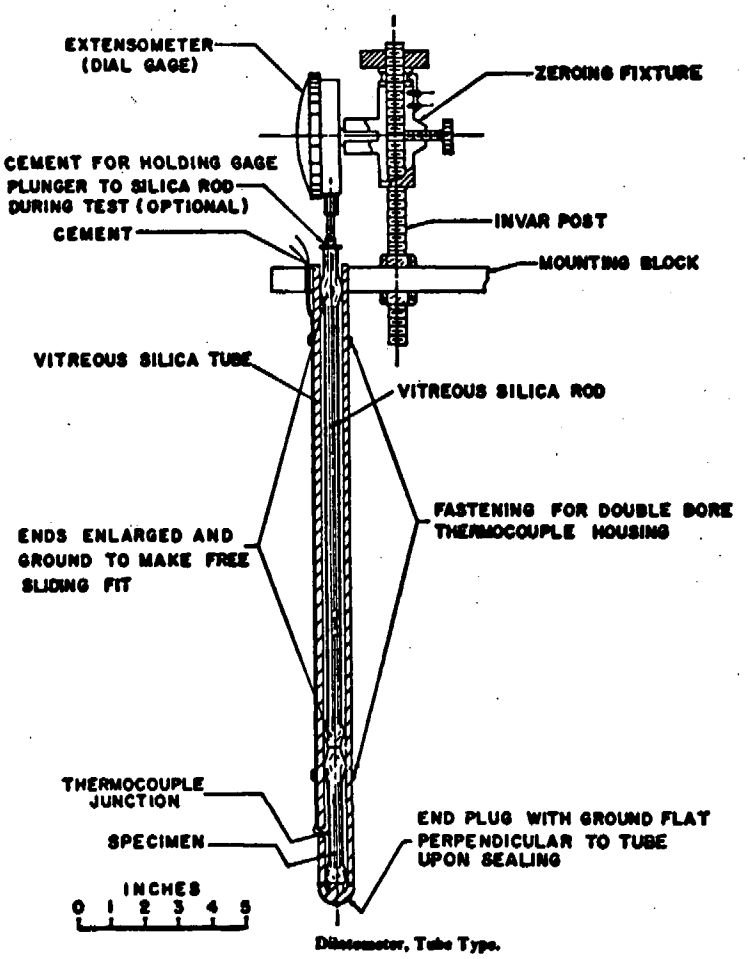

Fig. 1 - 1
ASTM
E 228 - 271

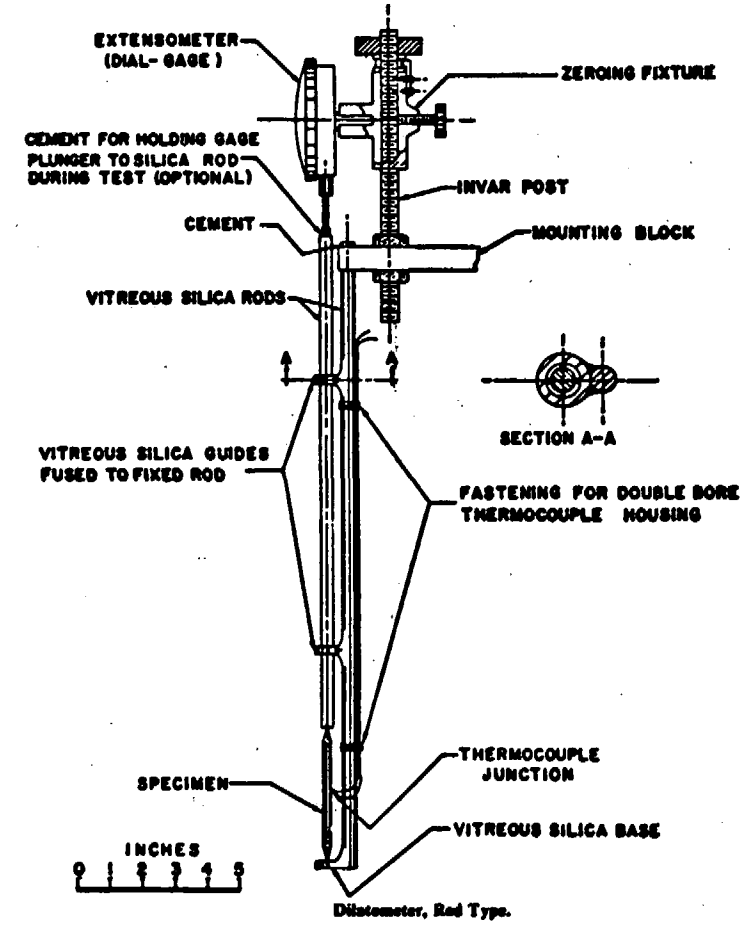

Fig. 1 - 2
E 228 - 71

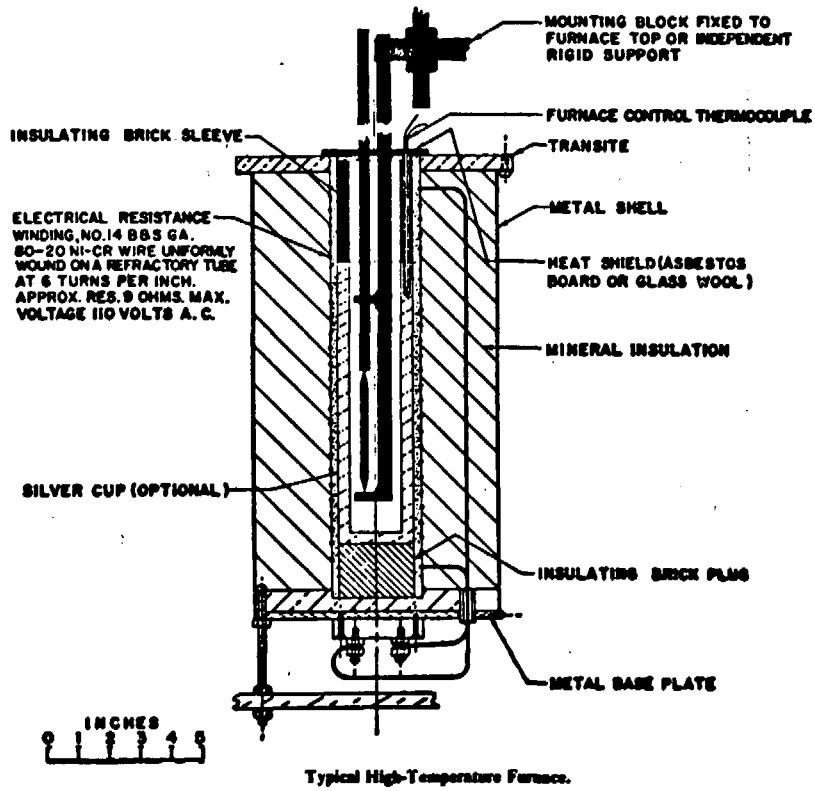

Typical High-Temperature Furnace.

Fig. 1 - 3
ASTM
E 228 - 71

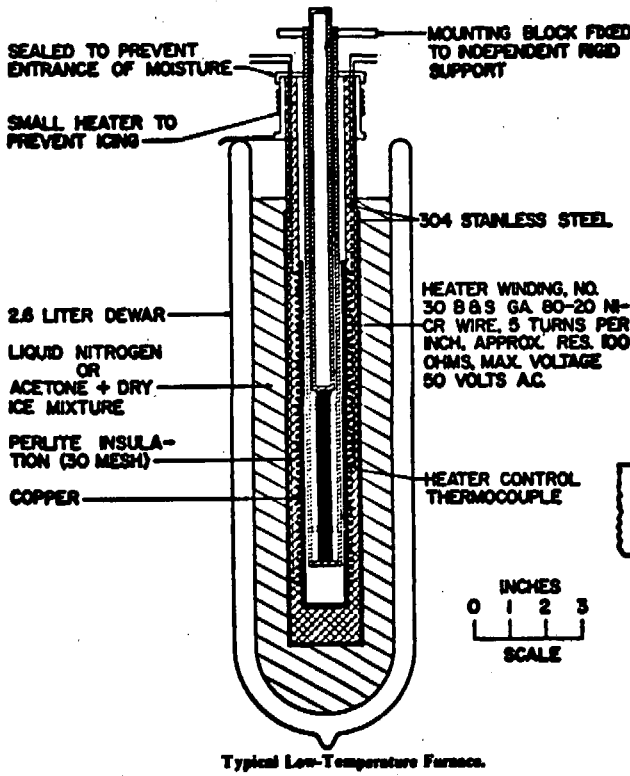

Typical Low-Temperature Furnace.

Fig. 1 - 4
ASTM E 228 - 71

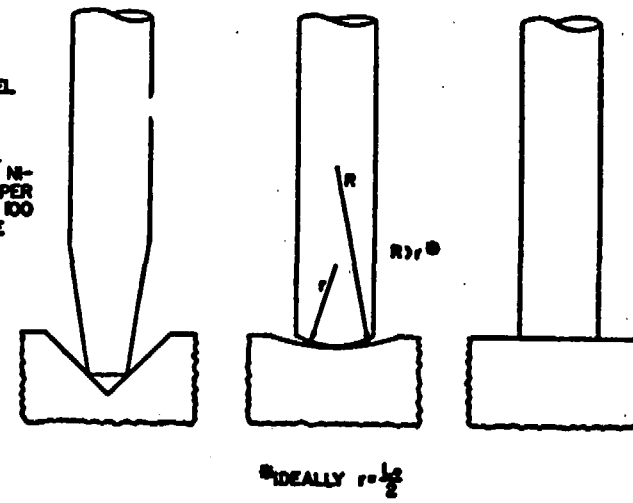

Shapes of Specimen Ends and Contact Surfaces.

Fig. 1 - 5
ASTM E 228 - 71

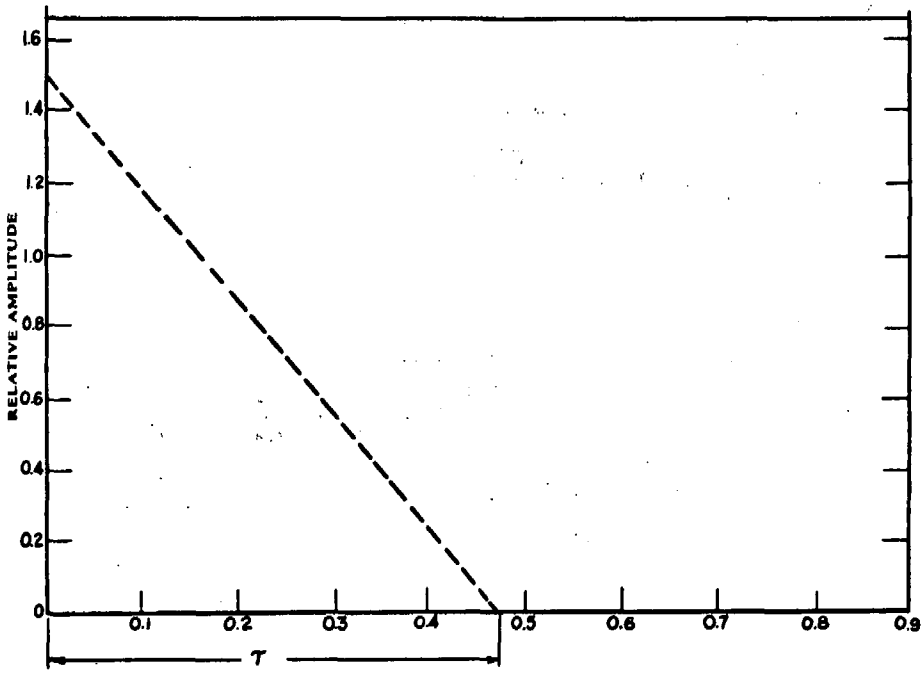

Flash Tube Response.

Fig. 2 - 1
ASTM
C 714 - 72

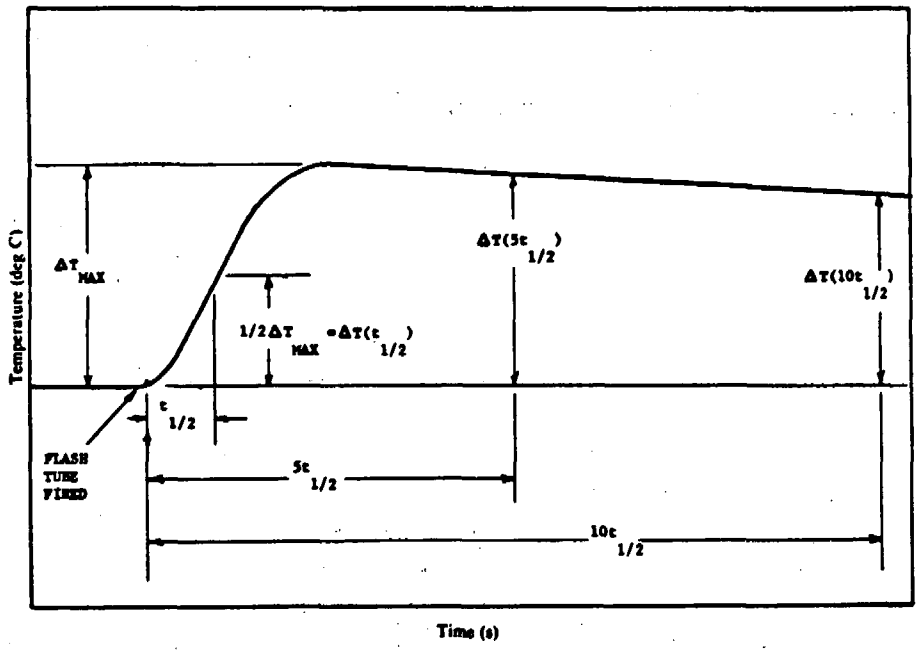

Example of Oscilloscope Trace Showing Parameters Used to Calculate Thermal Diffusivity.

Fig. 2 - 2
ASTM
C 714 - 72

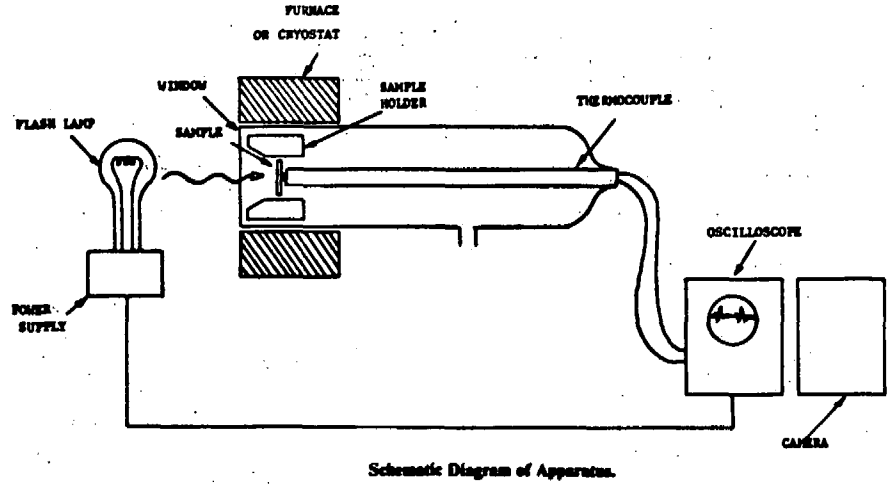

Schematic Diagram of Apparatus.

Fig. 2 - 3
ASTM
C 714 - 72

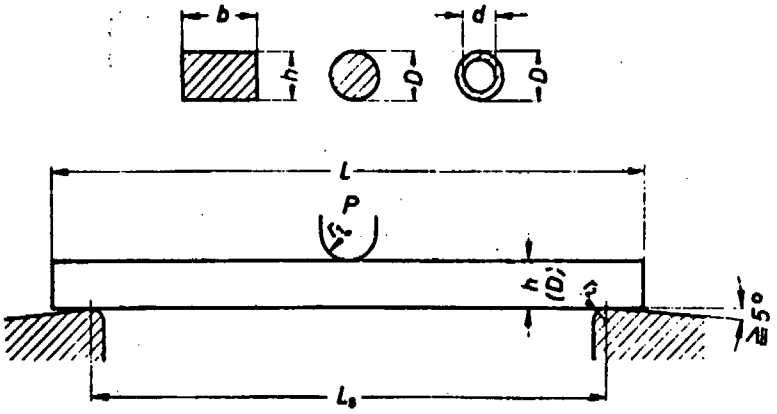

Fig. 3 - 1
DIN
53452

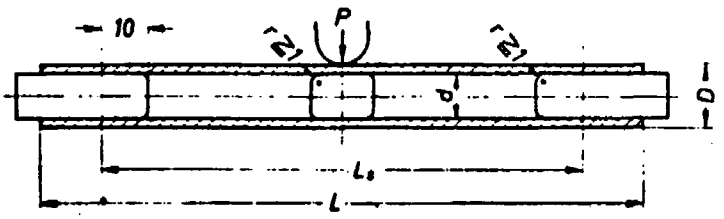

Fig. 3 - 2
DIN
53452

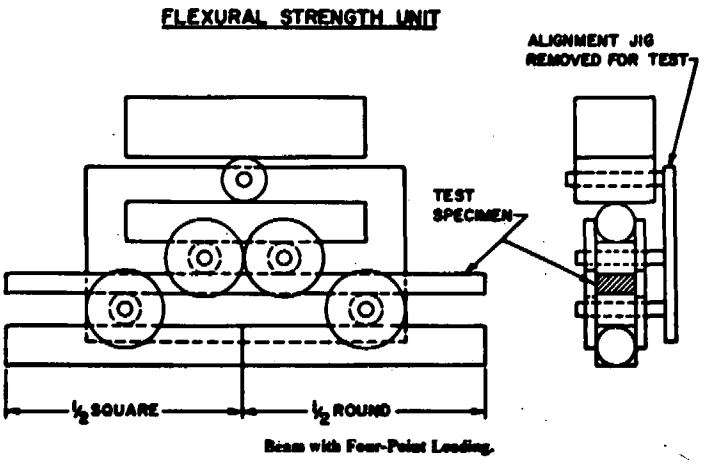

Fig. 3 - 3
ASTM
651-7o

3. Improvements in Characterization Methods of Pyrocarbon

by

H. Luhleich
K. Koizlik
E. Wallura
H. Hoven
M. Cremerius
J. Holliday
D.P. Frampton
Mrs. S. Allen
J.C. Hedderly

1. INTRODUCTION

Due to experimental work isotropic pyrocarbon layers as deposited in a fluidized bed are not a uniform material but consist of two components having different physical and chemical properties [1) 2)]:

-- one component of high density, strength and elasticity with a vitreous surface, called "HDC" (High Dense Component), and

-- the other of carbon black like appearance, called "CBC" (Carbon Black like Component).

Normally in a fluidized bed both of these two components are co-deposited, whereby the amount and the distribution of each component varies corresponding to the deposition conditions.

Based upon the different chemical and physical properties new characterization methods are developed [2) 3) 4)]. In the following paper the improvements of these methods - the plasma- and wetoxidation methods, the ultraonic method and the grinding method for the determination of density profiles - are described. Beyond it, first results of a further method, the scanning electron microscopy (SEM) are given.

2. PLASMA- AND WETOXIDATION METHODS

The different oxidation behaviour of the two components of pyrocarbon is used for the characterization of pyrocarbon especially of isotropic layers. Ceramographic sections of pyrocarbon coatings are etched by means of an oxygen plasma or an oxidative solution. For the characterization as well as possible both of these two procedures are necessary although the results of both are similar. During the wetoxidation process only a zone near the surface is etched whilst by the plasmaoxidation method it is possible to detect also lower areas. Therefore the wetoxidation method is more suitable for the determination of the amount of the CBC than the plasmaoxidation process. By means of the latter method the distribution of the CBC in the pyrocarbon layer is better to be seen than by the wetoxidation procedure.

It has been found that predictions can be made between the results of the oxidation etching methods and the irradiation behaviour of pyrocarbon layers of coated particles under normally used conditions for HTR's, viz. irradiation temperatures of about 1200°C and fluences of fast neutrons of about 5×10^{21} n.cm^{-2} ($E > 0.1$ MeV).

2.1 PREDICTION OF IRRADIATION BEHAVIOUR

The analysis of the relief structures of pyrocarbon layers developed by the oxidative etching processes is carried out by means of the following type scheme:

type 1 : layer structure of closed shells of HDC;
appearance after etching:
ring shaped elevations of HDC, and ring shaped hollows of CBC, the elevations of HDC continuous and unpierced.

Remark:
The presence of a continuous ring shaped hollow on the etched section normally is coupled with a continuous ring shaped unpierced HDC shell above or under it.

type 2 : layer structure of pierced shells of HDC;
appearance after etching:
continuous ring shaped elevations of HDC but pierced by channels of the CBC.

type 3 : layer structure with an inhomogeneous distribution of the CBC;
appearance after etching:
the distributions of cavities of the CBC is inhomogeneous.

type 4 : layer structure with a homogeneous distribution of the CBC;
appearance after etching:
the distribution of cavities of the CBC is homogeneous.

Of course one has to take in consideration that there are transitions between these types, and that there are pyrocarbon layers with two or more of these schematic structures. However, normally it is relative easy to associate the pictures after etching with the different structure types.

A good irradiation behaviour can be predicted for pyrocarbon coatings if there is

-- a structure of pierced HDC shells (type 2), and/or

-- a homogeneous distribution of the CBC and the HDC (type 4).

There is a further essential condition for a good irradiation behaviour of pyrocarbon layers:

The amount of the CBC must be sufficient. For surviving neutron irradiation under normal conditions the amount of the CBC should be at least 20 % of a layer area.

2.2 SPECIFICATION TESTS

The aim of further improvements has been the development of the etching methods as specification tests. For this purpose at first an internal standard was created, then a test certificate, and a handbook of etching pictures have been made. Other efforts were directed to determine the amount of the CBC quantitatively.

2.2.1 Internal standard

It has been turned out that especially in the case of plasmaoxidation the development of the relief structures relatively strong depends on the experimental conditions like high frequency energy interference, oxygen pressure, sample position in the reaction chamber etc. To eliminate these effects 2 sorts of coated particles with different outer pyrocarbon layers are added to each sample. The qualities of these two particle sorts were chosen under the following points of view:

-- the quantity of the particles is sufficient,
-- the coating layers of each sort are as equal as possible,
-- the etching time of the 2 sorts of pyrocarbon layers is different,
-- the structures after the etching process are different.

Fig. 1 shows the ceramographic sections of standard I before (Fig.1a) and after the plasmaoxidation procedure stepwise up to 40 min (Fig. 1b-e). Fig. 2a-d reproduces the same for the wetoxidation method. For each step the etching time was 1/2 min. The pyrocarbon layer of standard II is more resistent against oxygen attack than standard I. Therefore the etching time was longer. The results of the plasmaoxidation are shown in Fig. 3, those of the wetoxidation in Fig. 4.

2.2.2 Test certificate

To simplify the testing procedure a special test certificate has been worked out. Fig. 5 and 6 reproduce the test certificate, which is written in english and german. The most important structure types are described schematically. The testing results can be marked with a cross, viz. the testing procedure is time- saving.

2.2.3 Handbook of etching pictures

Because unexperienced persons have difficulties to correlate pictures and schematic structures, and therefore also to predict the irradiation behaviour of the pyrocarbon layers a handbook of etching pictures has been compiled. All sorts of particles included in the handbook have been irradiated. Fig. 7 and 8 show the front and backside of a leaf. At the head of the front page the marking of the particle batch, the most important production and characterization data, and the irradiation conditions are summed. Then the plasmaoxidized ceramografic section, a schematic presentation of it, and the corresponding structures of the test certificate follow. The back side contains the wetoxidized ceramographic section, the estimate of the CBC content, and the prediction of the irradiation behaviour in accordance with the test certificate. Finally by comparison the real irradiation behaviour is given. It is planned to enlarge this collection.

2.2.4 The quantitative determination of the CBC content

The CBC content of a pyrocarbon layer is determined quantitatively using wetoxidized ceramographic sections.
At KFA Jülich a first experiment was made by use of a "picture analyzer" (Bildanalysator T.A.S., Leitz, Wetzlar, Germany-West). Due to the width of the measuring area of 10 µm the determination has been made stepwise. Fig. 9 shows a part of the wetoxidized section containing the measuring area of the "picture analyzer". Beside the photo the values of the CBC content in % related to the total area of the measuring area are reproduced. Clearly the picture and the printet values show an inhomogeneous distribution of the CBC in the pyrocarbon layer. If a good irradiation behaviour is demanded the average of 18,5 % for the CBC content is too low.

2.3 Collaborative Work at Dragon Project

At Dragon Project work has proceeded on the basis of close collaboration with KFA on the etching of pyrocarbon structures using techniques previously described by Luhleich et al [2], with emphasis on the wet-oxidation method which has now been established as a routine. Work has now commenced on developing a simplified equipment for the plasmic oxidation etching technique using the principle involving the direct bombardment of the pyrocarbon surface

with positive oxygen ions. A prototype equipment has been constructed based on the Penning cold cathode discharge equipment described by Holland [12] and illustrated in Figure 17. Preliminary results are promising [13] and an improved equipment is now being built.

2.3.1 Quantifying the Carbon Black Component (CBC) in a Pyrocarbon Layer

Work is now proceeding on an investigation into the usage of a photographic contour technique developed by Agfa Gavaert Ltd. and known in proprietory terms as Agfakontor. Etched pyrocarbon when photographed under normal brightfield illumination reveals, in most cases, the CBC as a dark area in a lighter matrix of High Density Carbon (HDC). The normal photographic contrast between the CBC and HDC is not sufficient for measuring purposes, but if a highly contrasted contour effect could be obtained then some quantification could be achieved.

2.3.1.1 Basic Principles of Agfakontor

In photography equi-densities are the planes of equal density in a photographic original. If the density of the original is measured point by point using a densitometer and the points of equal density are joined by a line, it has the effect of breaking down the image in much the same way as contours are used in cartography. The equi-densities of a photographic original can be rendered visible by copying on Agfa Contour Film.

Equi-densities reproduced by Agfa contour film are classified according to their equi-density width and equi-density position as follows.

Equi-density Width refers to the density range of the original covered by the Agfa contour film. This width can be altered by the use of yellow filters. The bigger the yellow filter factor the narrower the equi-density range, and if desired the equi-density can be widened if a magenta filter is used.

Equi-density Position can be changed within the density range of an original by changing the exposure time (fixed yellow filtration). There is a regular association between the density of the original at which the equi-density should appear, and the exposure required.

2.3.1.2 Preliminary Results on Pyrocarbon Layers

First experiments have shown that if an original film of a wet-oxidised pyrocarbon layer was exposed on to an Agfa contour film, variation in yellow filtration and exposure times can produce a range of changes in photographic contrast between the CBC and HDC components in the layer. Some success has been achieved in contrast enhancement, but some difficulty was also experienced in eliminating light spots within the dark CBC areas. It is suggested that this difficulty can be overcome if hard lithographic film is used as the original which would tend to eliminate light spots in the CBC at the first stage of the process. The photographic examples shown in Figures 18 and 19 illustrate the drastic changes in contrast which can be achieved. Figure 18 is a photomicrographic print of a sample of etched pyrocarbon photographed under normal brightfield illumination, Figure 19 is the same original photograph exposed onto Agfa contour film.

2.3.1.3 Quantifying CBC Content Form an Agfa Contour Print

The visual appraisal of change of contrast as shown in Figure 19 is simple, the CBC and HDC areas are easy to identify and could be quantified on a precentage basis. The same visual examination of the example shown in Figure 18 is rather more difficult and any quantitative assessment would be very painstaking. The percentage assessment of CBC and HDC as shown in Figure 19 would be very simple if an image analysing computer such as a Quantimet 720 were used, with a high degree of accuracy, but if the same computer were used to examine Figure 18, the errors in its assessment would probably be unacceptable. Work is continuing in this field, and it is hoped to assess a large number of etched samples using the contour process together with a Quantimet, before arriving at conclusions regarding the effectiveness of the process, all that can be said at this stage is that it appears to be a useful aid to quantitative ceramography.

2.4 Future Collaborative Work

Other methods of characterisation of pyrocarbon are already well known and include the measurement of geometric parameters such as shape, and coating thickness. These are usually documented in testing manuals, or in the case

of Dragon Project, DPR 731 [14] is frequently used as a testing method reference in the various specifications. The Project and KFA have agreed that no satisfactory method seems to exist for defining and measuring shape, and in the case of many other parameters such as density, anisotropy and uranium contamination profiles, much needs to be done to improve the state of knowledge of what effects (of the properties or parameters being measured) have on performance, and what are the effects of all, or of each property on parameter with each other on performance.

3. ULTRASONIC AND GRINDING METHODS

Due to the fact that pyrocarbon contains two components it was argued that a separation by means of a physical method is possible. This proved to be true and ultrasonic[a] vibration turned out to be the best method for separating the two components. In the beginning coated particles have been treated with ultrasonic and the amount of extracted material has been related to the whole coating layer [5]. Soon it could be demonstrated that in most cases the removed CBC only originates in the outer part of the layer. Therefore the ultrasonic treatment and a stepwise mechanical grinding technique used for the analysis of uranium in pyrocarbon coatings [6] has been combined for the determination of the CBC content in pyrocarbon layers, and the drawing up of CBC profiles.

Furthermore the grinding method has been used to measure the density of pyrocarbon layers stepwise, and to get density profiles.

3.1 Description of apparatus

Fig. 10 represents a sketch of the ultrasonic apparatus. It consists of a high frequency generator connected to a bath filled with methanol containing the vibrator. During the ultrasonic treatment the methanol bath was held at a constant temperature of 25°C by water cooling.
The coated particles were put into a rectangular glass cell of an electrophotometer (length 5 cm, width 1,8 cm, heigh 4 cm) which was filled with methanol (23,5 ml) up to a calibration mark. The closed glass cell was placed into the methanol bath of the ultrasonic generator.

After ultrasonic vibration the concentration of the extracted CBC in the methanol of the glass cell has been determined by measuring the optical extinction with an electrophotometer described ealier [5].

The coated particles were grinded mechanically in special glass containers stepwise [7]. These containers were cylindrical glass tubes with

a hemisperical bottom, and rough surfaces of the inner walls. Four of these glass containers were fixed into a mill and the particles were grinded by rotation (Fig. 11).

3.2 Experimental routine for the determination of the CBC

The coating layers of a fixed amount of coated particles with a total surface of 420 mm^2 were removed by grinding in steps of 5 to 20 µm. In the beginning and after each grinding step the coated particles were cleaned 5 min by an ultrasonic treatment. Then the particles were put into the glass cell filled with methanol and vibrated by ultrasonic for about 60 min.

The amount of the CBC, which was extracted by the ultrasonic procedure has been calculated by weighing the dry particles before and after each grinding step.

3.3 Experimental routine for the determination of density profiles

The pyrocarbon coating of a fixed amount of coated particles was removed in steps of about 10 µm. In the beginning and after each grinding step the length of this quantity of coated particles in file and its weight has been measured and of it the average of the diameter and the weight of one coated particle was calculated. The length of the coated particles in file has been determined by the V-slot method [8]. The accuracy of this method is about 1 µm. The weight has been determined with an accuracy of about 1 µg. The apparent density was calculated by the calculated volume of the abraded material and its weight.

3.4 Results

Fig 12a shows the rough distribution of the CBC in an HDI pyrocarbon coating layer, viz. a CBC profile determined by the combined ultrasonic and grinding methods, and by comparison Fig 12b represents the density profile. Those parts of the pyrocarbon layer having a high CBC content correspond to low densities and vice versa. These results are also in accordance with the plasmaoxidation result shown in Fig. 12c. Layer parts with a high CBC content also correspond to hollows in the plasma-oxidized surface of the coating layer.

4. SCANNING ELECTRON MICROSCOPY

During the last years, a new electronic equipment, the scanning electron microscope, has become available in structural analysis of pyrocarbon. Although it does not reach the high resolution of a transmission electron microscope (TEM), the SEM has under certain conditions considerable advantages compared to the TEM. Most important seems to be that the samples which are to be examined are more or less untreated surfaces or areas produced by breaking a sample. Fig.13 and 14 e.g. show a typical pyrocarbon surface with a "cauliflower" structure at low (Fig.13) and high (Fig.14)magnification.

On the other hand, TEM needs very thin cuts of pyrocarbon normally reached by thinning a section by e.g. argon ion bombardment. Since one knows from plasmaoxidation that the poorly cristallized CBC is removed from the sample more easily than the HDC one should expect that, under ion bombardment, pyrocarbon behaves similar. Thus the interpretation of TEM micrographs can be very complicated.

The first systematic experiments with the SEM on the field of pyrocarbon structural analysis show, in any case, its very good usefullness. Three main tasks are treated with the SEM today:

--- basic research concerning the deposition mechanism and the two component model of pyrocarbon,

--- analysis and classification of morphology of pyrocarbon surface in search of a correlation between other material properties and deposition conditions on the one hand and this morphology on the other, and, at last,

--- use as a high magnification, high resolution microscope to visualize the surface structure of pyrocarbon after plasmaoxidation treatment.

In most cases the SEM is used as a high magnification, high resolution microscope, beeing, with respect to its efficiency, between the optical light microscope and the TEM. But for some other problems its ability to produce micrographs on the basis of orientation contrast or material contrast is of high interest. So, for example, first results of material contrast analysis of pyrocarbon coatings of fuel particles by the SEM confirm the assumption of the CBC to be removed more quickly than the HDC by plasmaoxidation.

For the moment, main field of operation is the basis research on deposition mechanism of pyrocarbon following the pyroaggregate conception [1) 9)10)]. Very interesting results could be found, which are reported elsewhere [11)]. Just two further examples shall give an idea of possible results of pyrocarbon deposition. Fig. 15 shows statically deposited "pseudowhiskers" (magnification x200), and Fig. 16 the first stage of deposition, beginning in the inner region and the edges of a groove in the substrate (magnification x300). Both phenomena can be well interpreted by the pyroaggregat conception.

ABSTRACT

Based upon the two component model of pyrocarbon the improvements in characterization methods - the plasma- and wetoxidation methods, the ultrasonic method, and a grinding method for the determination of density profiles - are described. The application of the plasma- and wetoxidation methods to specification tests is discussed. Beyond it, first results of a further new method, the scanning electron microscopy (SEM) are given.

References

1. H. Luhleich, and L. Sütterlin, ATKE 14 293 (1969)

2. H. Luhleich, L. Sütterlin, H. Hoven, and H. Nickel, and
H. Luhleich, and L. Sütterlin, DPTN/307 (QCWP/P.35), Apr. 1972

3. H. Luhleich, L. Sütterlin, H. Hoven, and H. Nickel, Z. Anal. Chem. 255, 97-103 (1971)

4. H. Luhleich, H. Büsch, H. Hoven, L. Sütterlin, and E. Wallura, CARBON '72, Preprints p. 144, Baden-Baden (Germany) 25.-30.6.1972

5. L. Sütterlin, H. Büsch, H. Luhleich, H. Nickel, and H. Hoven, Berichte der Kernforschungsanlage Jülich, Jül-798-RW (1971)

6. E. Wallura, Berichte der Kernforschungsanlage Jülich, Jül-989-RW Aug. 1973

7. E. Wallura, J. Rottmann, H. Nickel, E. Gyarmati, and R. van Sinay, Berichte der Kernforschungsanlage Jülich, June 1971

8. R.L.R. Lefevre, DPRDD 1751, Oct. 1968

9. L. Sütterlin, Berichte der Kernforschungsanlage Jülich, Jül-735-RW, 1971

10. L. Sütterlin, G. Haag, H. Luhleich, H. Nickel and P. Pflaum, Preprints CARBON '72, p. 273, Baden-Baden (Germany) 25.-30.6.1972

11. K. Koizlik, J. Linke, H. Luhleich, H. Nickel, P. Pflaum, Berichte der Kernforschungsanlage Jülich, to be published

12. L. Holland and N. Sutherland, Edwards High Vacuum Research Report No. 117.

13. C.L. Wrench, Etching of Pyrolytic Carbon in a Penning Cold Cathode Discharge, DPTN/373.

14. J. Holliday et al., Methods for the Pre-irradiation Examination of Low Enriched UO_2 HTR Fuels, DPR/731.

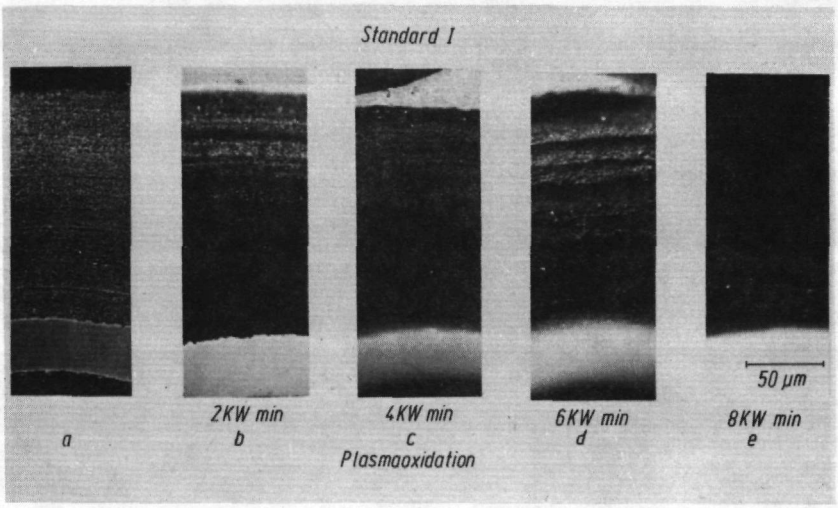

Fig. 1 Ceramographic Sections of Standard I
(a) before and
(b) - (e) after Plasmaoxidation Stepwise

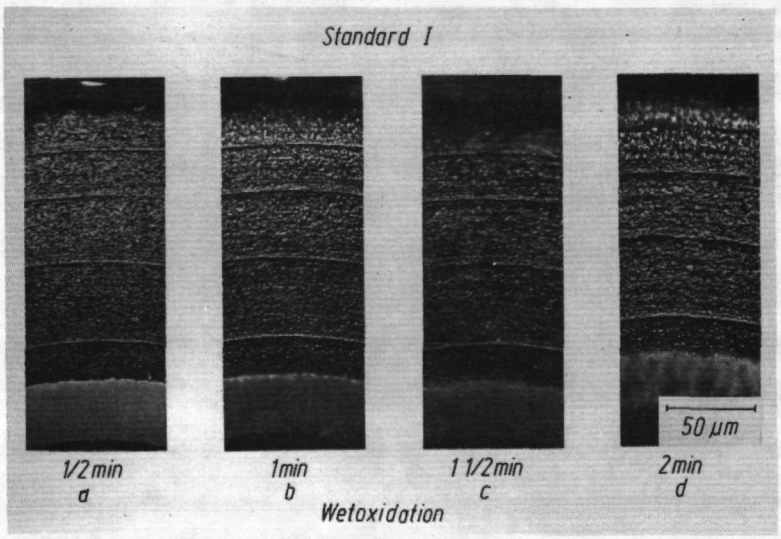

Fig. 2 Ceramographic Sections of Standard I
after Wetoxidation Stepwise (a) - (d)

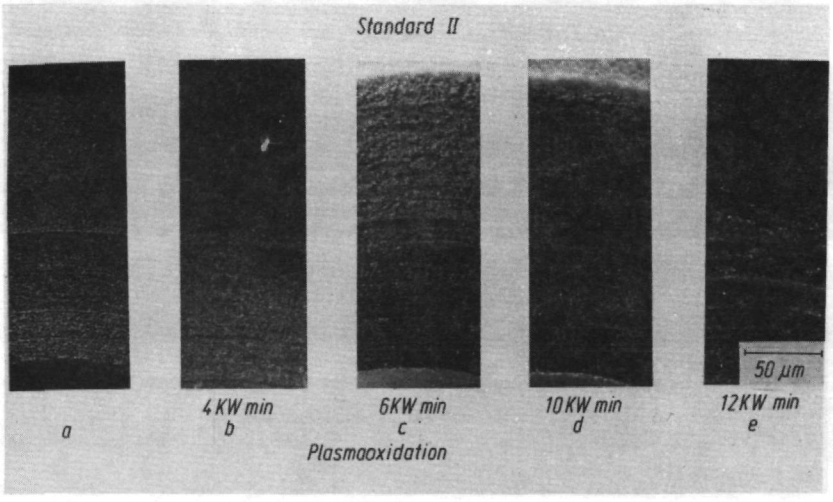

Fig. 3 Ceramographic Sections of Standard II
(a) before and
(b) - (e) after Plasmaoxidation Stepwise

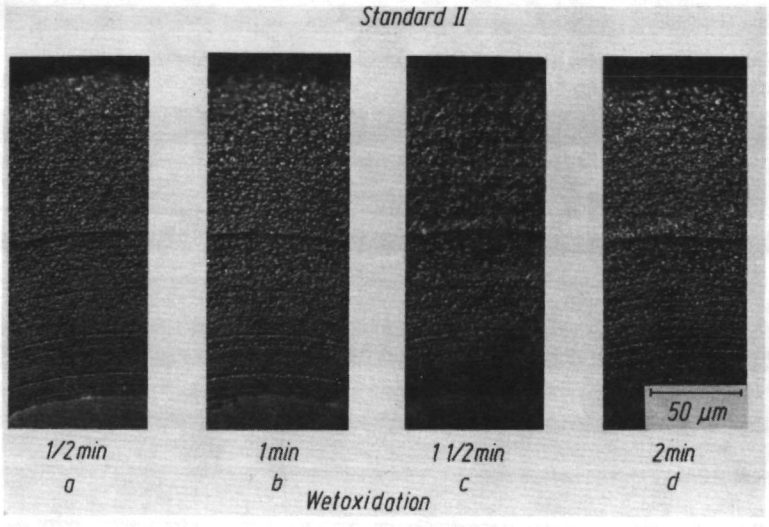

Fig. 4 Ceramographic Sections of Standard II
after Wetoxidation Stepwise (a) - (d)

Fig 5 Test Certificate (Page 1)

PLASMA- and WETOXIDATION
Plasma- und Naßoxydation

RESULTS of CHARACTERIZATION
Charakterisierungsergebnis

sample
Probe .....

unirradiated ☐ irradiated ☐
unbestrahlt bestrahlt

plasmaoxidation ☐ oxidation steps .....
Plasmaoxydation Oxydationsschritte .....
(min/watt) .....

wetoxidation ☐
Naßoxydation

remarks
Bemerkungen: .....
.....

layer structure homogeneous
Homogener Schichtaufbau

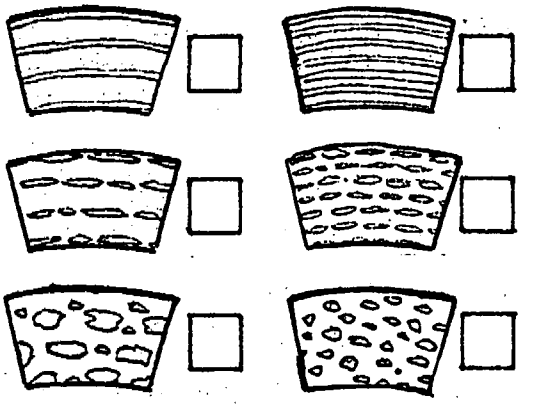

layer structure inhomogeneous
inhomogener Schichtaufbau

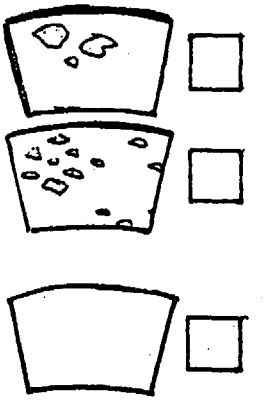

insert special structures
Zum Einzeichnen spezieller Strukturen

layer structure composed of two or more different layer parts
Schichtaufbau aus 2 oder mehr unterschiedlichen Schichtteilen

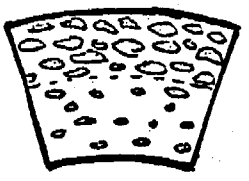

☐ CBC content in the outer part > in the inner part of the layer
CBC-Gehalt im Außenschichtteil > im Innenschichtteil

☐ CBC content in the inner part > in the outer part of the layer
CBC-Gehalt im Innenschichtteil > im Außenschichtteil

Fig. 6 Test Certificate (Page 2)

CBC content
CBC-Gehalt :

very large / sehr hoch : ☐ large / hoch : ☐ sufficient / genügend : ☐ small / gering : ☐ very small / sehr gering : ☐

IRRADIATION BEHAVIOUR
Bestrahlungsverhalten:

predicted / vorausgesagt :	good / gut :	☐	medium / mittelmäßig :	☐	bad / schlecht :	☐
real / tatsächlich :	good / gut :	☐	medium / mittelmäßig :	☐	bad / schlecht :	☐

section No. / Schliff-Nr. : .....

photo No. / Bild-Nr. : .....

registration No. / Ablage-Nr. : .....

..... (testing position) (Prüfstelle)

..... (date) (Datum)

..... (examiner) (Prüfer)

PLASMAOXIDATION

Leistung El. Power : 200 W
Atzzeit Etching Time : 30 min

PyC : Propen (C_3H_6)

Bestrahlungs Experiment	Irradiation Experiment:	DFR-P3 BR2-P10	
Beschichtungs Temperatur	Deposition Temperature:	1350	°C
Aufwachsgeschwindigkeit	Deposition Rate :	423	µm/h
Dichte	Density :	1,96	g/cm³
BAF	BAF :	1,05	

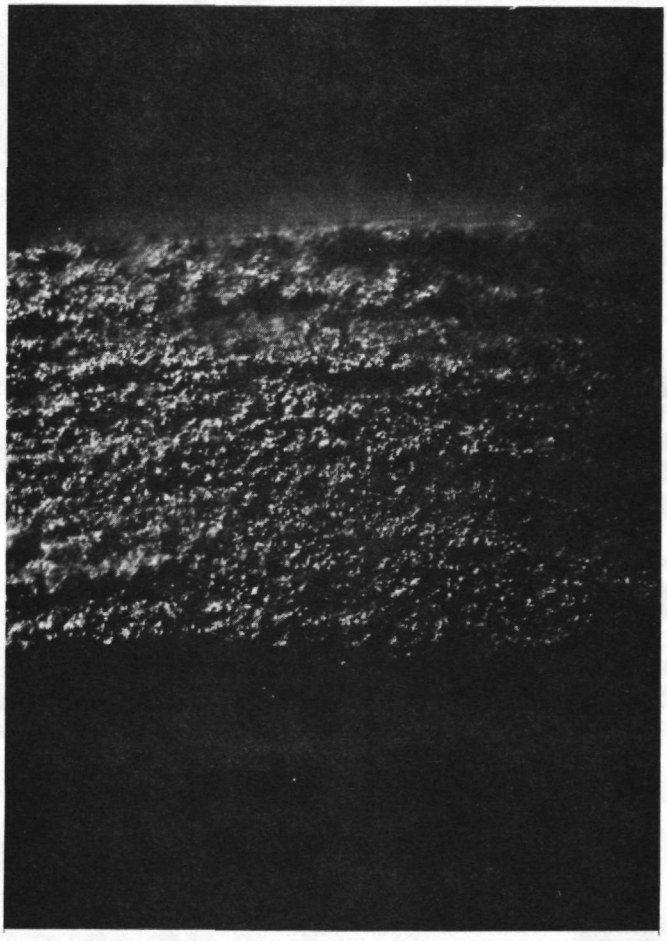

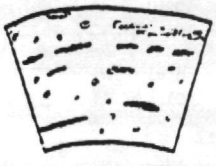

Schematische Darstellung
Schematic Graph

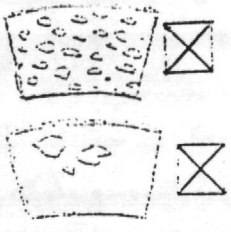

Prüfungsprotokoll
Test Record

Fig. 7 Page of the Handbook of Etching Pictures (Front)

NASSOXIDATION WETOXIDATION

Elektrolyt Electrolyte : $K_2Cr_2O_7 - H_3PO_4$
Ätzzeit Etching Time : 1min

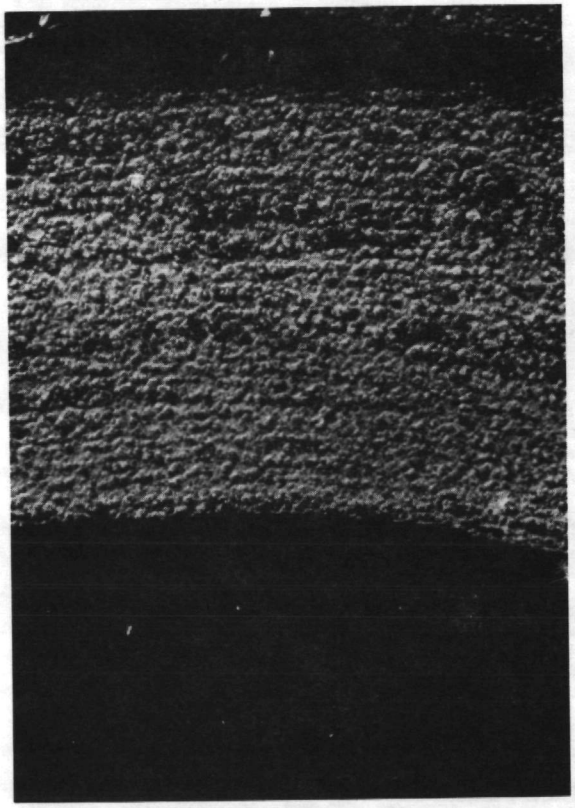

CBC content
CBC-Gehalt :

very large / sehr hoch : ☐ large / hoch : ☒ sufficient / genügend : ☐ small / gering : ☐ very small / sehr gering : ☐

IRRADIATION BEHAVIOUR
Bestrahlungsverhalten:

predicted / vorausgesagt :	good / gut :	☒	medium / mittelmäßig :	☐	bad / schlecht :	☐
real / tatsächlich :	good / gut :	☒	medium / mittelmäßig :	☐	bad / schlecht :	☐

Bestrahlungs Temperatur	Irradiation Temperature	: 1200	°C
Abbrand	Burn up	: 12.7	% FIMA
Fluenz	Fluence	: 6.8	10^{21} cm^{-2} E 0,1MeV
Defekt	Defective	: 0	%

Fig. 8 Page of the Handbook of Etching Pictures (Backside)

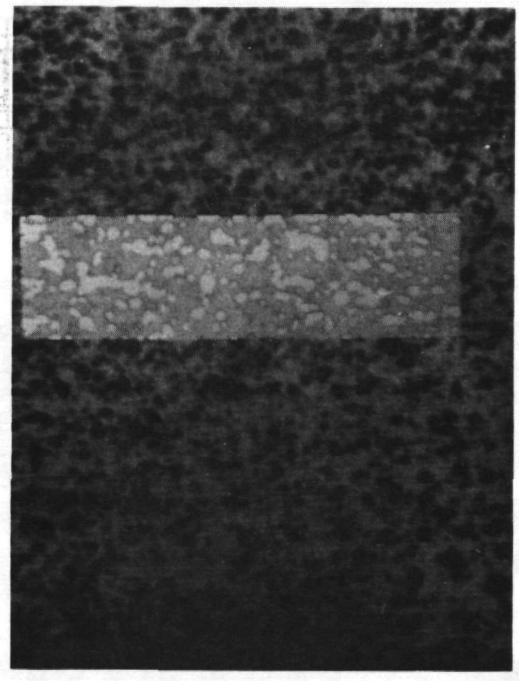

Fig. 9 Wetoxidized Ceramographic Section with Measuring Area of the "Picture Analyzer"

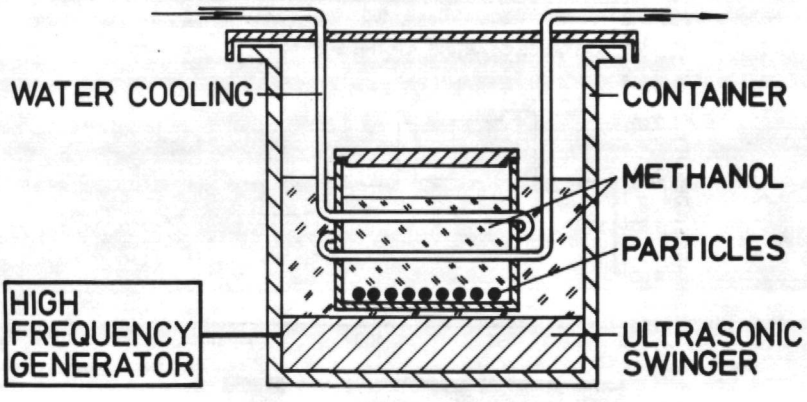

Fig. 10 Sketch of the Ultrasonic Apparatus

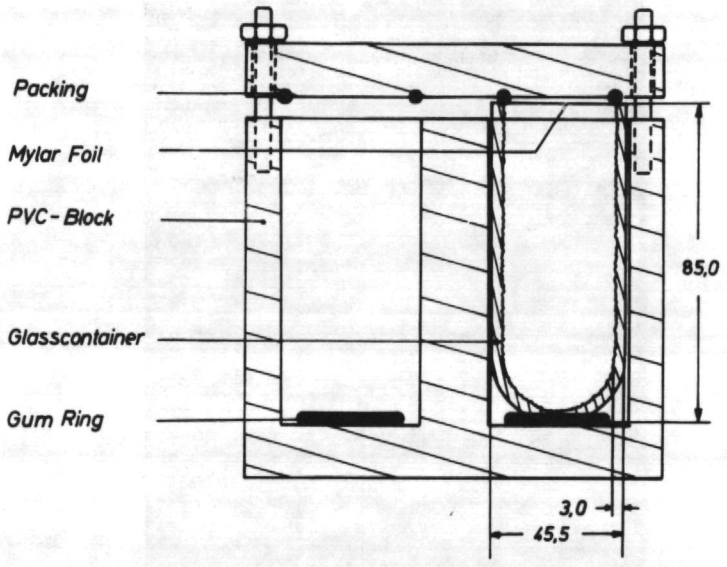

Fig. 11 Schematic Presentation of the Apparatus Used for the Grinding Technique

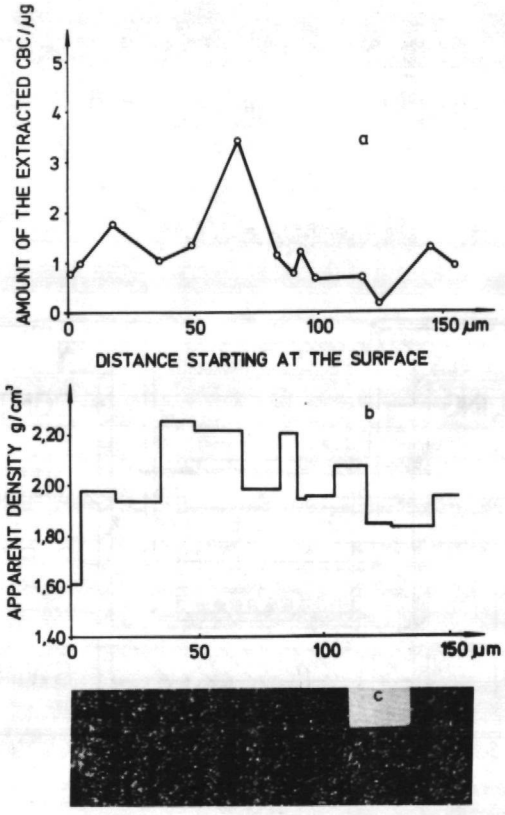

Fig. 12 Results of the Combined Ultrasonic and Grinding Techniques:
(a) CBC Distribution Profile
(b) Density Profile
(c) Plasmaoxidized Section

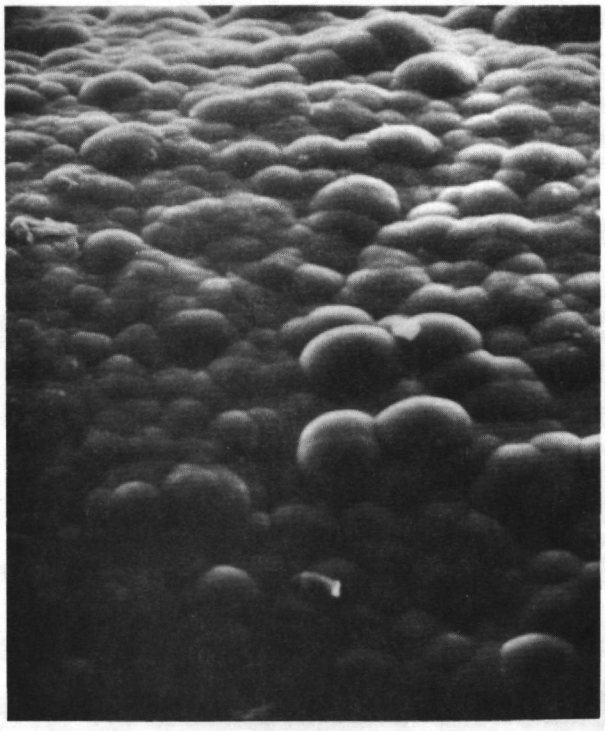

Fig. 13 Surface of Statically Deposited Pyrocarbon (CH_4, T = 2400°C), Magnification x 300

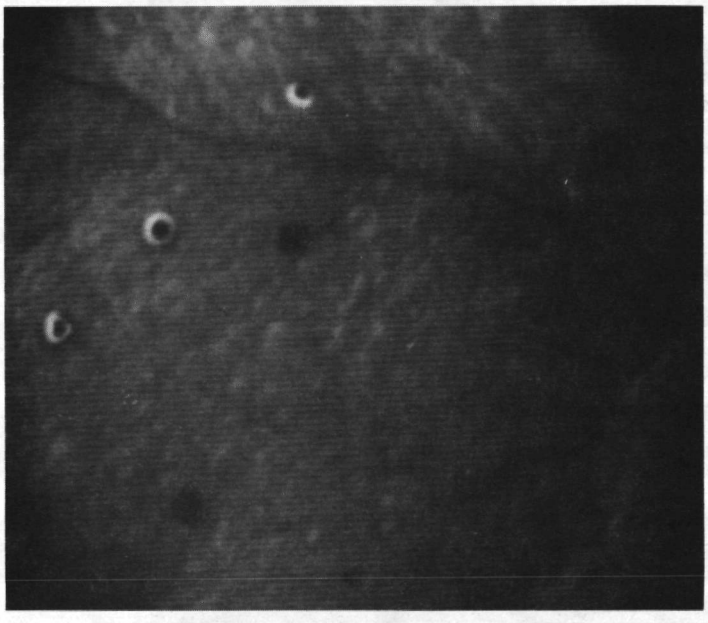

Fig. 14 The Same Sample as in Fig. 13, but Magnification x 10 000. The Structure with a Size of about 1000 Å Can Well be Seen

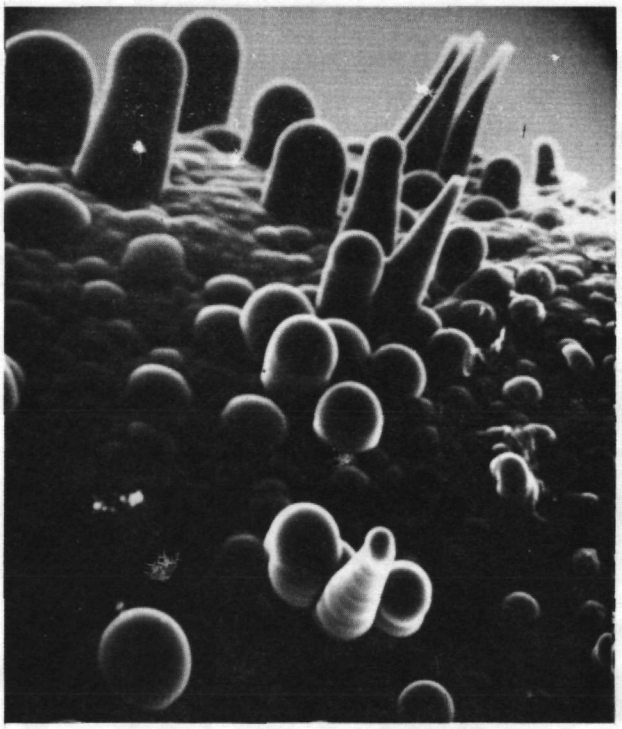

Fig. 15 Statically Deposited Pyrocarbon Showing "Pseudowhiskers" (CH_4, T = 2400°C) Magnification x 200

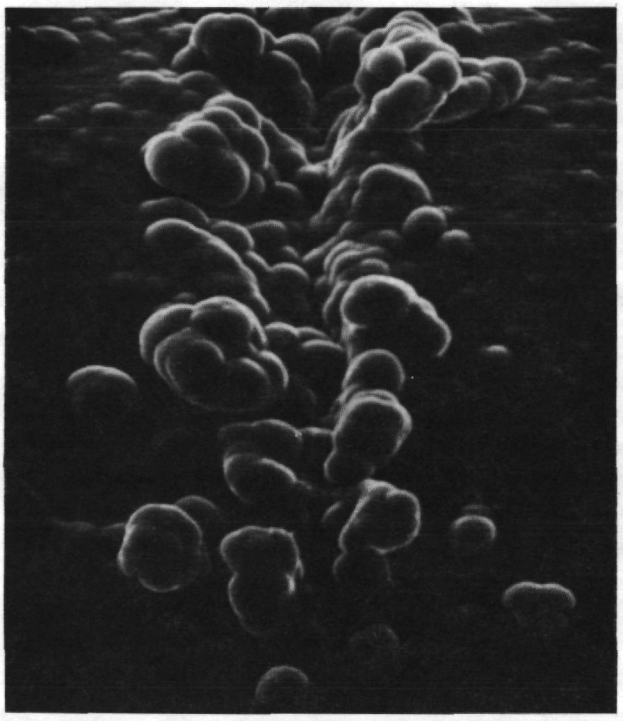

Fig. 16 Statically Deposited Pyrocarbon, Deposition Beginning on the Walls of a Groove in the Substrate (CH_4, T = 2300°C), Magnification x 300

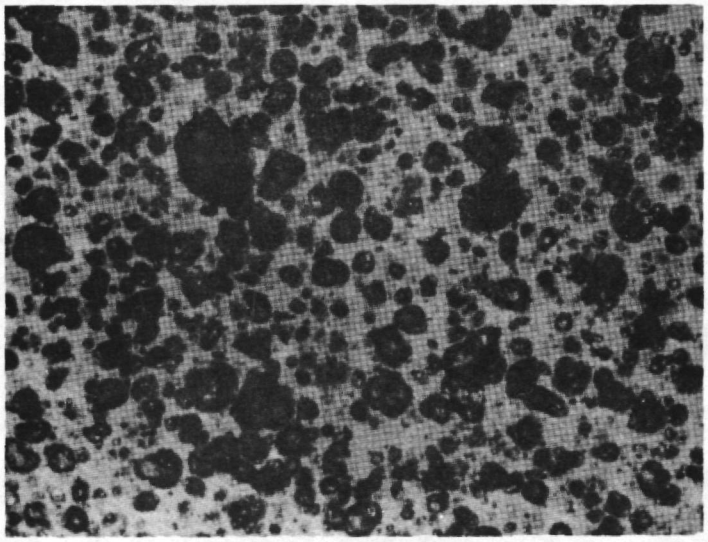

FIG.18: Etched Pyrocarbon (Wet Oxidation)
Brightfield Illumination X 1000.

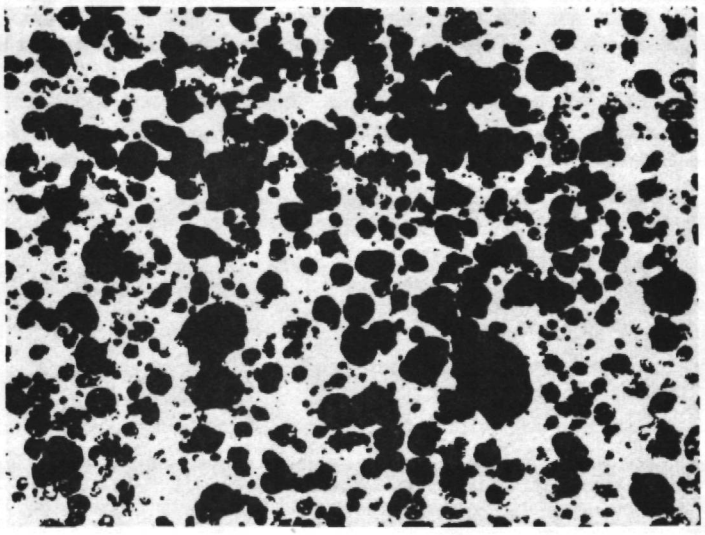

FIG.19: Fig.18 Copied on AGFA-CONTOUR FILM X 1000.

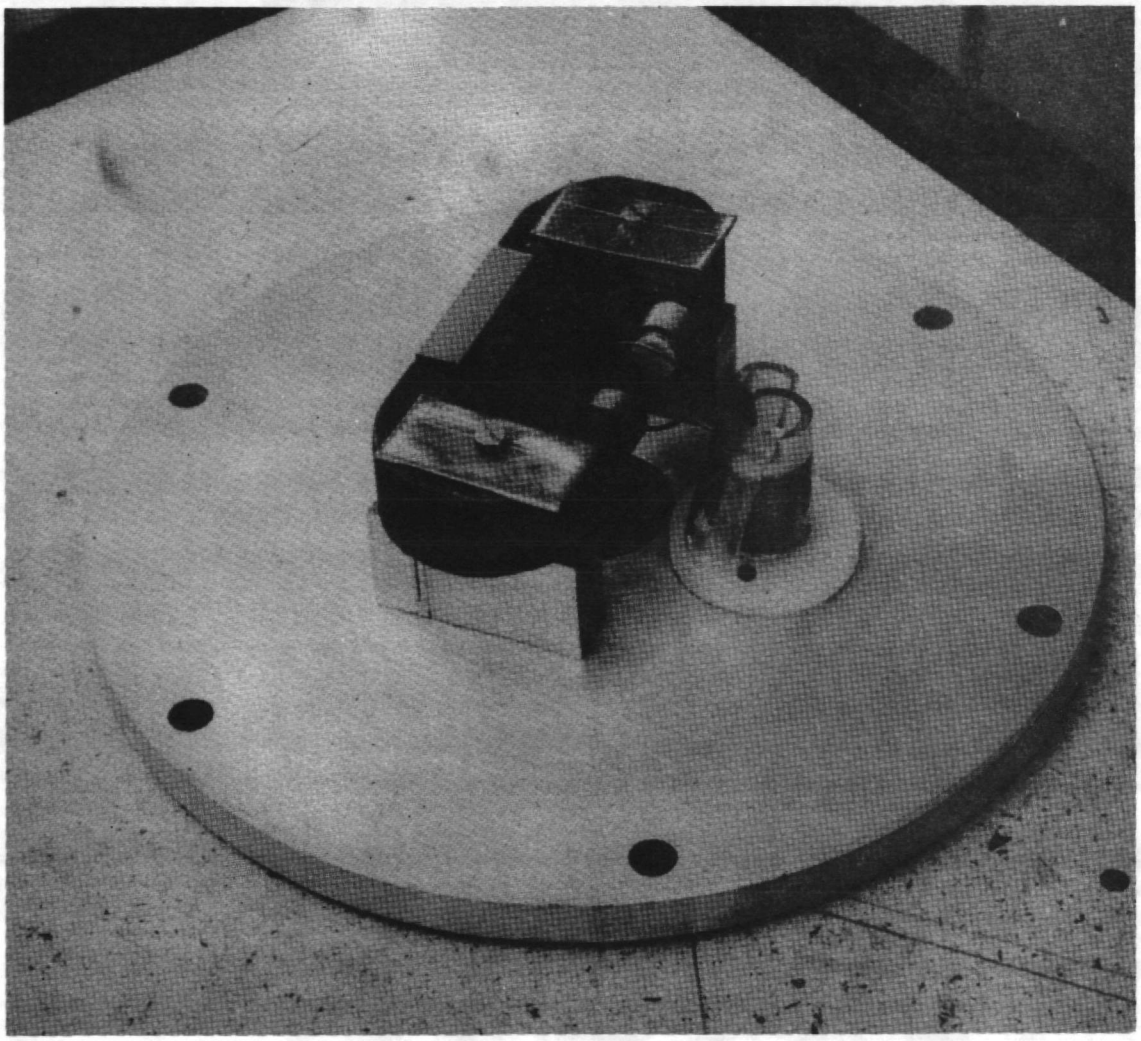

Fig. 17: Prototype equipment for simplified plasmic oxidation etching technique

4. Determination of Strength and Young's Modulus of Pyrocarbon - and Siliconcarbide Layers of Coated Fuel Particles

by

K. Bongartz

H. Schuster

K. Täuber

Summary

A method to measure strength and Young's Modulus on SiC- or PyC-ring-specimens prepared out of coating material deposited on HTR fuel particles was developed by KFA recently. By this method difficulties in the interpretation of the measured values which arise for instance if measurements are performed on materials deposited on discs should be avoided. Stress calculations for the coating of particles with SiC interlayer have shown that during the end phase of irradiation the SiC layer has to carry the main load. Therefore the mechanical properties of the SiC are mainly responsible for the mechanical integrity of the whole coating of the particle. For that reason mainly SiC properties have been measured so far. As simple rings are employed in the measurement the mathematical analysis is easy, no significant corrections are necessary.

1. Preparation of Specimens

For the preparation of the rings a particle with SiC-interlayer is polished from two opposite sides until a disc remains, as is indicated on the left side of figure 1. From this disc the kernel can be removed and the PyC is separated by chemical oxidation. The photograph on the right of figure 1 shows a scanning-electron-microscopic picture of a SiC ring.

2. Measurement

The rings are measured and deformed diametrically between two parallel sapphire plates as is shown schematically on figure 2. With the breaking load and the ring geometry the strength, and with the load-deformation-diagramme Young's Modulus can be calculated. The mathematical formalism for these calculations is known. When an entire ring is employed in the test the maximum stress which is identical with the rupture stress appears at the inner surface of the ring in point A, see left side of figure 2. Davidge [1] could show that rupture in SiC starts always at the surface, which means that the strength of SiC depends on the properties at the surface which sees the maximum load. For a complete characterisation of the material it is therefore necessary to check if the outer surface gives different values for the strength.

For this purpose deformation measurements are performed on halfrings, as is shown schematically on the right side of figure 2. Here the maximum stress appears at the outer surface in point A.

Can the strength values derived before be presented as final results ?

3. Evaluation and Results

Rupture of a ring is a typical example of brittle fracture. The measured values of the strength show a material-inherent statistical distribution for which to our present knowledge the best prediction can be derived from the statistical theory of Weibull. From this theory it follows that the rupture stress measured at different specimens of one material depends on the geometry and stress distribution over each specimen during the test. In the case of our ringshaped specimens pressed diametrically between two plates this distribution is non-uniform having a strongly pronounced peak in the points A. Now we want to know the rupture stress of the SiC shell on the coated particle under uniform stress distribution. Weibull's theorey allows to calculate it from the rupture stress measured on rings.

The table shows results for the strength and Young's Modulus of SiC of two typical particle sorts. The rupture stress measured on rings $\sigma_{Z\ ring}$, the calculated equivalent strength of the spherical shell $\sigma_{Z\ spherical\ shell}$ and Young's Modulus E are given. These values are derived from measurements on halfrings and entire rings as well. We see that there is a clear difference between the rupture stress which can be attributed to the inner and the outer surface. Besides, the sort number 488 has higher strengths.

Figure 3 shows the structure of both SiC layers. It shows photographic enlargements of a diametrical section through a segment of a ring and the surfaces of the ring in the scanning electron microscope. It can be seen that the grain size on the right sort is smaller and that the grain size in each layer encreases from the inside to the outside. The results of the measurement becomes evident if start of fracture in the surface is assumed which depends on the grain size of the material below the surface. It appears that a small grain size of the material results in high strength. In figure 4 the strength is plotted versus the deposition temperature. Here this tendency is confirmed, because the finest grain results from the lowest deposition temperature. Furthermore the grain size may be reduced when during deposition the fluidization gas hydrogen is diluted by a carrier gas e.g. Argon. This tendency shall be confirmed by further measurements.

It should be mentioned that very high values can be obtained for the strength. We get maximum values attributed to the spherical shell of a particle layer of 1ooo MN/m^2. This value is not a chance hit as can be seen from figure 5. The figure shows the rupture stresses of the rings in a Weibull plot. The

theory predicts that the points should ly on a straight line. The results of 98 rings are plotted. The wide scatter of the results is of great technical interest. For the allowable probability of fracture of 10^{-4} the Weibull theory gives a value for the strength of 320 MN/m^2 (with m = 9, m = Weibull-Parameter).

4. Reference

1) R.W. Davidge et al.: Strength of pyrolytic SiC coatings for high-temperature gas-cooled reactors. Journal of the American Ceramic Society, Vol. 56, No. 1, Jan. 1973

Particle Sort		468		488	
Deposition Temp. [°C]		1500		1400	
Density [gcm^{-3}]		3.21		3.21	
Measuring Method		Half Ring	Entire Ring	Half Ring	Entire Ring
Number of Specimens		76	53	76	98
E	$\frac{MN}{m^2}$	440 · 10^3	350 · 10^3	590 · 10^3	470 · 10^3
σ z ring		980	1540	1220	1890
σ z spherical shell		540	670	750	970

Table: Mechanical Properties of SiC as Coating Material

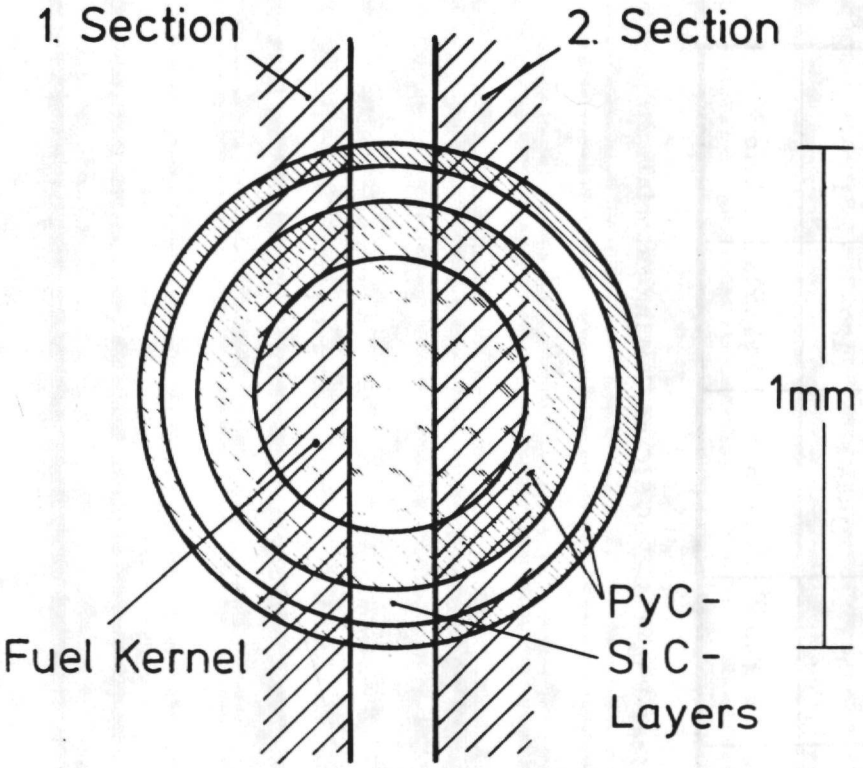

Preparation

SEM-Picture

of a SiC-Ring

Fig. 1: Specimen for Ring Test

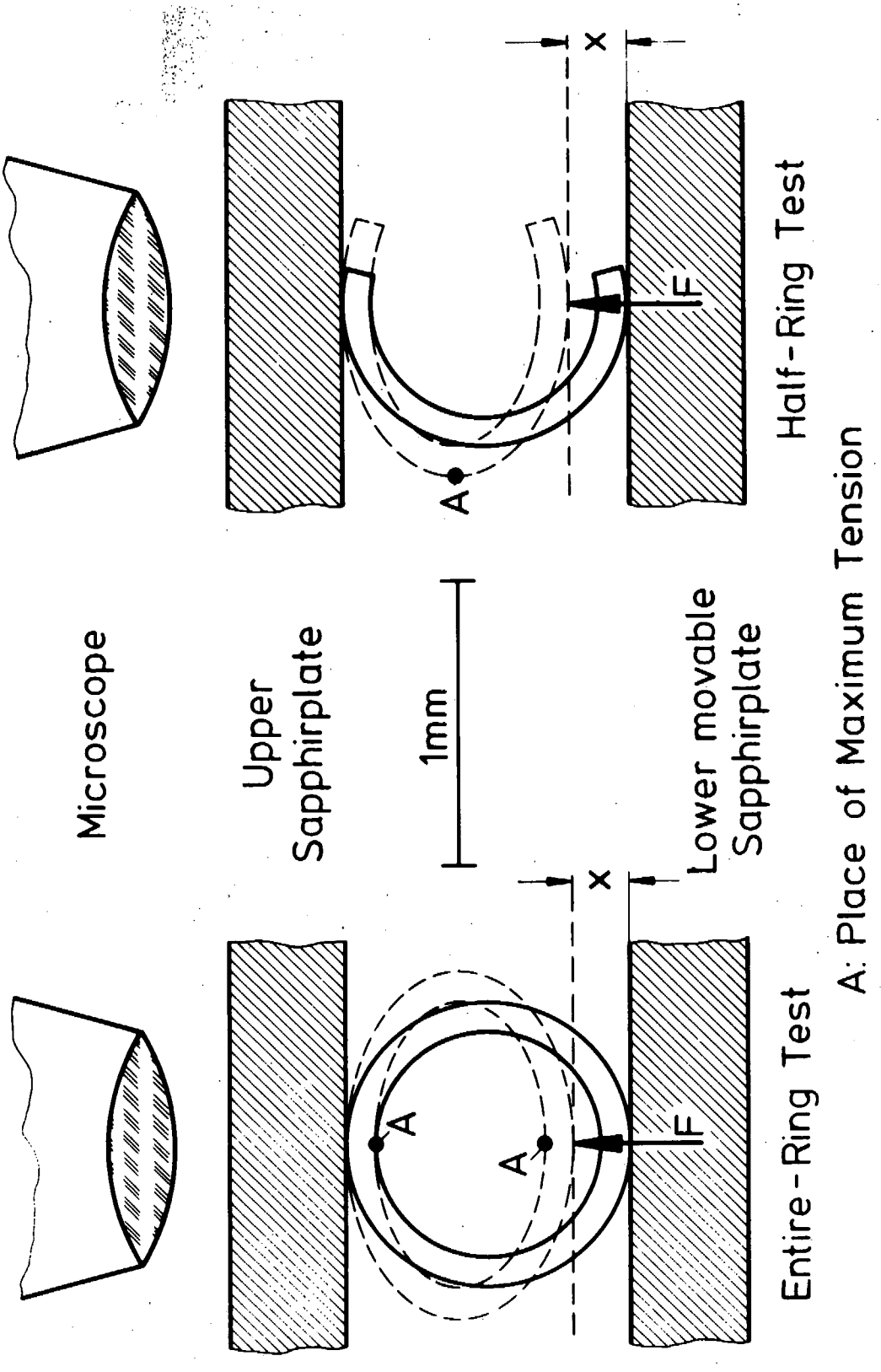

Fig. 2: Ring Test

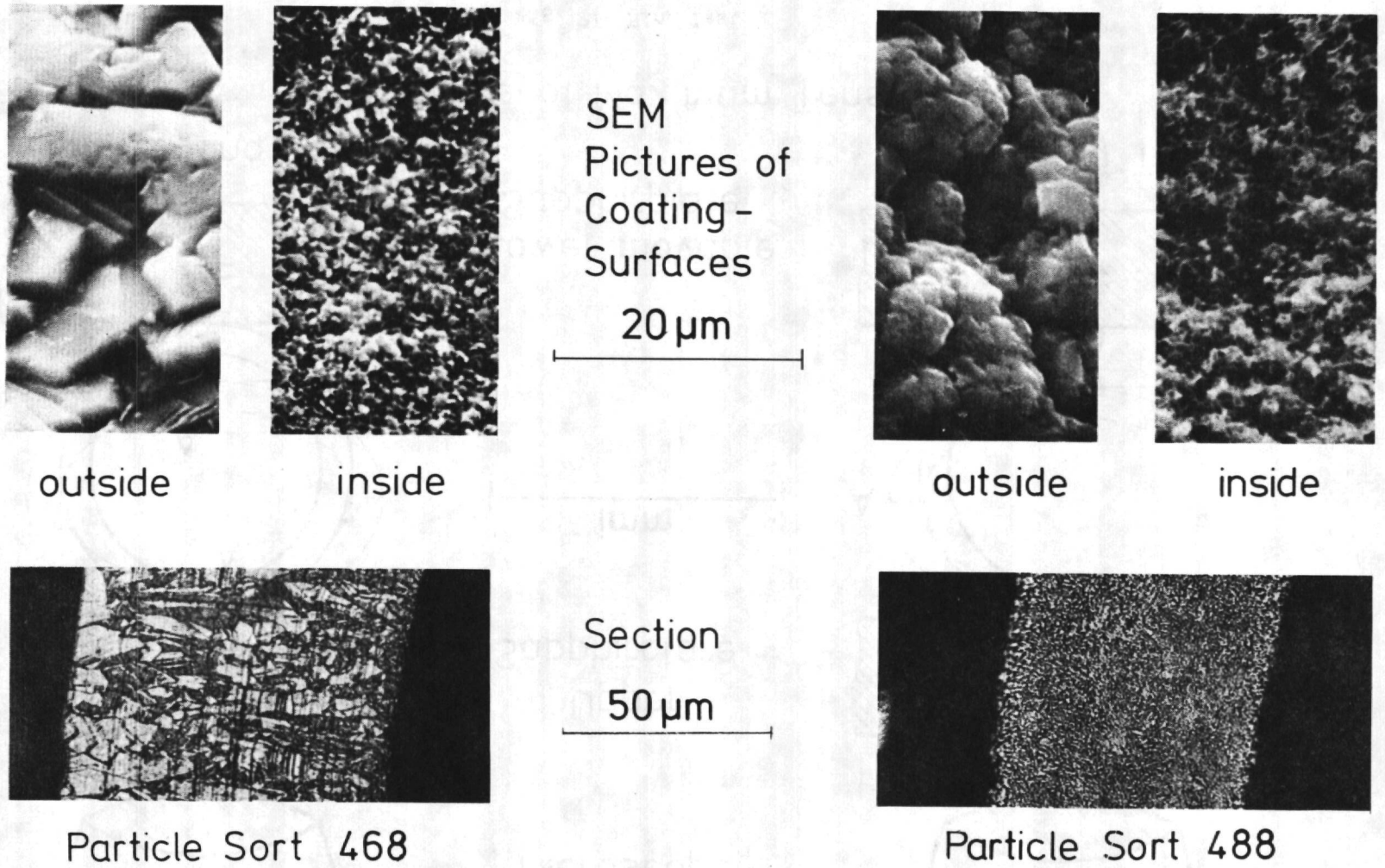

Fig. 3: Microscopic Pictures of SiC Coating Layers

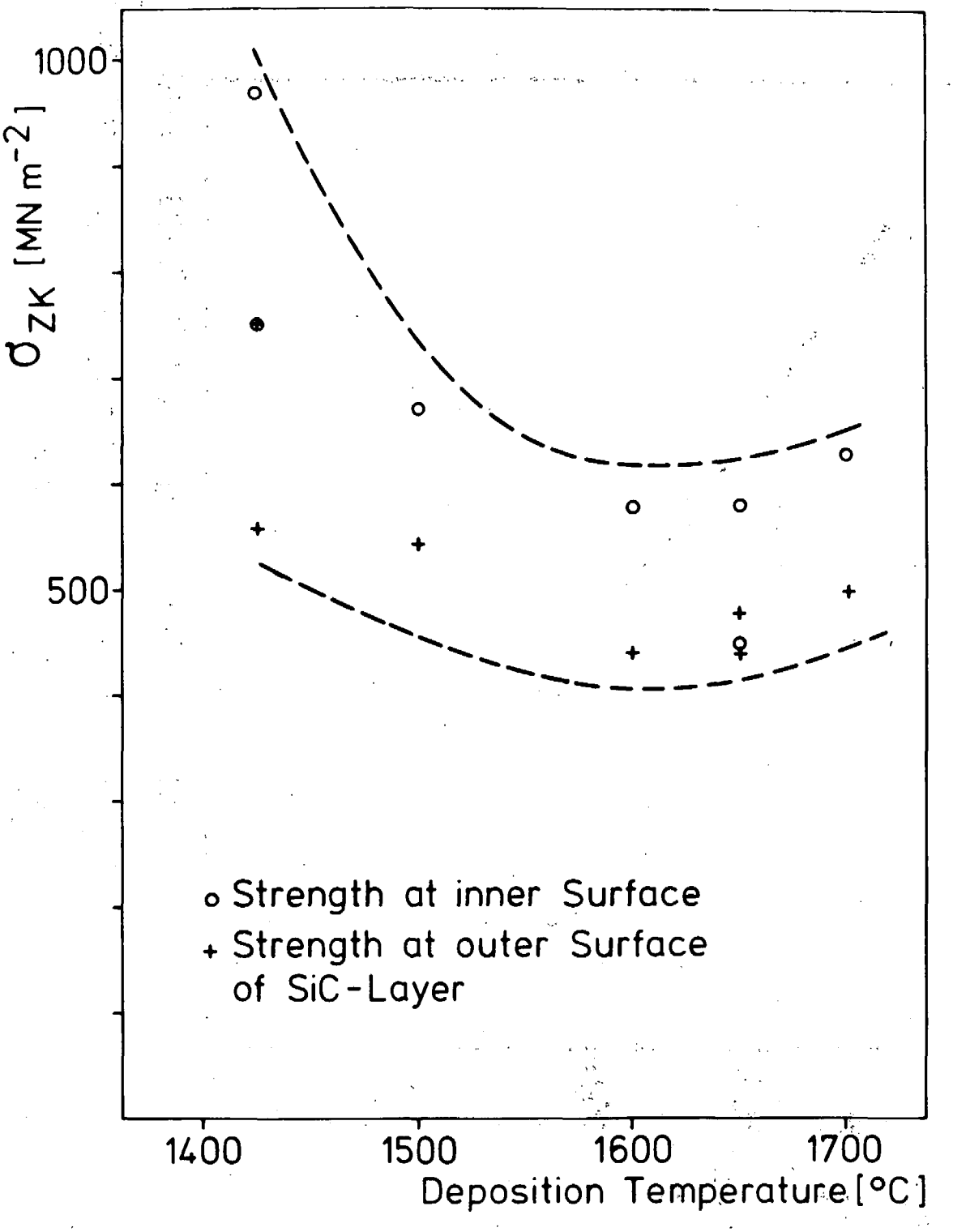

Fig. 4: Strength of SiC Coating Layers

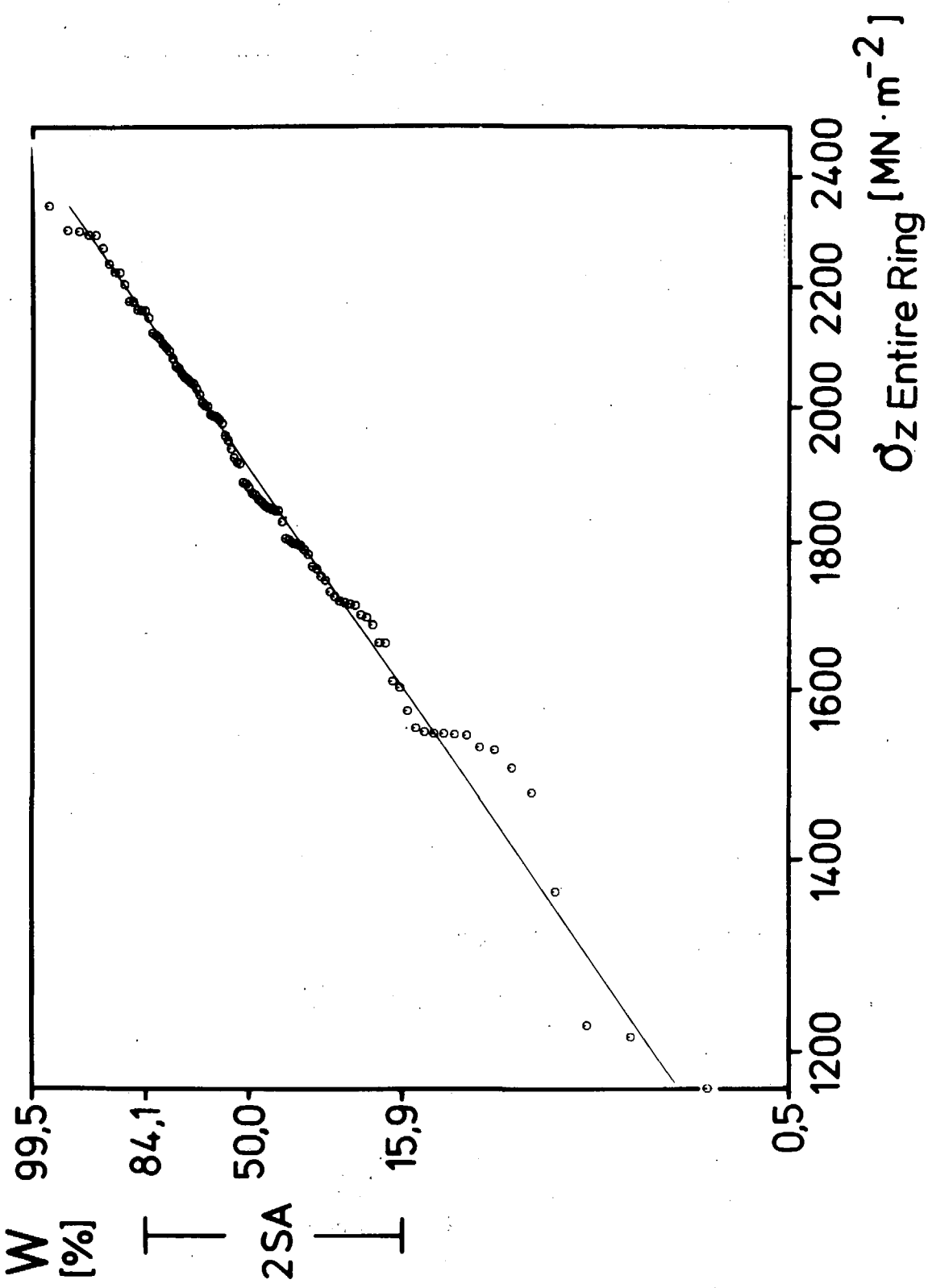

Fig. 5: Strength of SiC Rings in Weibull Plot
(Particle Sort 488)

5. Microporosity

A Characteristic Property of Pyrocarbon Coatings

by

P. Krautwasser

1. Introduction

Fuel elements for high temperature gas cooled reactors comprise graphitic materials as the structural element and embedded fuel in form of pyrocarbon coated particles. The pyrocarbon is deposited on the fuel kernels by pyrolytic decomposition of gaseous hydrocarbons, such as methane and propene. The structure and therefore the physical and chemical properties of the deposits vary in a wide range, depending on the deposition conditions, among which deposition gas, temperature, and deposition rate are the most important.

The main objective of the coating is to retain the fission products generated during reactor operation. This implies, that the pyrocarbon coanting must remain intact during the life-cycle of the fuel particle in the reactor. The behavior of the particles during an irrdiation test, roughly described by the failure rate of particles, the release of fission products, and the visual inspection of ceramographic sections, depends very heavily on the original state of the pyrocarbon and is therefore a function of the deposition parameters. Unfortunately, the deposition mechanism is very complex, and the comparison between the deposition conditions and the irradiation behavior cannot be made directly, but only by means of characterizing the material after deposition.

Because of the small size of the samples, the usual methods of material testing cannot be employed on the pyrocarbon coatings. To date, the most significant characterization factors have been density and anisotropy and the visual inspection of ceramographic sections. Although, these methods yield information about the optimal range of the deposition parameters, they are not sufficient to fully describe the coating, as has been demonstrated by recent studies of characterization by use of plasmaoxidation, TEM and microporosity measurements.

If a pyrocarbon coating remains intact during an irradiation test, it means that either the coating can sustain high stresses or the increase in stress, caused by the fission gas pressure and the irradiation induced dimensional changes, is rapidly reduced by microphysical rearrangement of the material. The characterization measurements presently used have been unable to describe the microscopic state of the coating or the microscopic changes occuring during irradiation, or inversely, the influence of the microstructure on the irradiation behavior. The microporosity, being a component of the microstructure, gives important information on the microscopic state of the material and allows a quantitative correlation between the deposition parameters and the microstructure of pyrocarbon. Therefore, it is possible to associate the optimal deposition conditions, empirically determined by numerous irradiation experiments, with the microstructure of the material, and inversely, to predict the irradiation behavior of a given pyrocarbon deposit. The main aims of our microporosity measurements are therefore:

a) to develop a new sensitive characterization method for pyrocarbon coatings which gives additional information on the material properties;

b) to study the influence of deposition parameters on the microstructure of the pyrocarbons;

c) to compare the microstructure with the irradiation behavior;

d) to associate the empirically specified deposition rate with a structural state of the pyrocarbon coatings;

e) to examine the change of the material during heat treatment and irradiation.

2. Measuring method

The evaluation of small angle x-ray scattering curves allows the determination of regions of diluted material with diameters of about 1o to 1ooo Å, which are referred to in the following as pores.

For x-ray analysis, the pyrocarbon layer is separated from the kernel or other layers by cracking the coated particles. The fractured pieces are put in a glassy capillary tube for x-ray examination. The measurements are performed with a Kratky x-ray small angle camera with $Cu K_\alpha$ irradiation. The scatterd intensity is registered with a proportional counter tube, discriminator, and Teletype. The scattering curve is corrected for collimation error, normalized for the weight per unit area of a standard sample, and the radii of gyration evaluated with the modified standard method.

3. Results

3.1 Sensitivity of the characterization method

As mentioned above, the material properties measured to date give information about the optimal range of the deposition parameters. But within this range, materials with different irradiation behavior often have nearly or exactly the same density and anisotropy. As an example, in Fig 1 the pore spectra of three propene-pyrocarbon coatings and a methane coating are plotted. The concentration of each pore size in the reference sample is normalized to 1oo %. Although the propene-pyrocarbons have exactly the same density and anisotropy of cristallographic orientation, the pore spectra are totaly different and vary up to a factor of eight. Therefore, it can be deduced that measurement of microporosity by x-ray small angle scattering is a sensitive characterization method, allowing the differentiation of pyrocarbons which could not be distinguished with the methods previously used.

3.2 Heat treatment of stressed and unstressed pyrocarbon coatings

Fig 2 shows the change of relative pore concentration for pore sizes of 1o to 1ooo Å in a low density propene-pyrocarbon treated 3 hrs at temperatures between 18oo and 28oo°C. The concentration curve for each pore size starts with the value of 1oo % representing the original state of the samples. A significant growth of the energetically preferred larger pores, which consume the smaller ones, can be noted. This results in a change of the maximum of relative pore concentration with increasing temperature to larger pore sizes. The increase in density from 1.4 to 1.7 g/cm^3 cannot be explained

solely by the reduction of the layer plane distance, C/2, from 3.497 to 3.400 Å. The small increase in density between 1400 and 2100°C relates to a decrease of the pore size fraction with diameters greater than 500 Å, probably due to crystallite growth. The apparent crystallite size, L_c, was observed to increase from 32 Å to 49 Å after 3 hrs at 2100°C and 148 Å after 3 hrs at 2800°C. Above 2100°C, only the fraction of pores up to about 40 Å in diameter decreases. Therefore, the observed increase in density has to be explained by small pores migrating to surfaces, boundaries or other sinks. This implies that nearly all of the porosity is associated with pores in the size range 10 - 40 Å, a proposition which is proved in part 3.5 of this paper.

Heat treatment of stressed pyrocarbon coatings showed the same porosity — temperature behavior; the pore concentration curves shifted to lower temperatures, which means that a part of the thermal energy is substituted by elastic energy. The creep processes in the coatings, caused by internal or external stresses during heat treatment, lead to a strong decrease of the smallest pores by the processes described for heat treatment. In Fig 3, the change of pore spectra during a heat treatment of 3 hrs at 2300°C is shown in curve a. The change during creep processes in the coating caused by internal CO/CO_2-gas pressure in the fuel particles is shown in curve b.

3.3 Influence of deposition parameters on the pore spectra

The pore spectra of propene-pyrocarbon coatings have been measured to examine the influence of deposition temperature and gas concentration, i.e. deposition rate. The deposition temperatures and gas concentration were respectively 1100, 1250, 1400, 1600, 1800, and 2000°C and 5, 10, 20, 40, and 60 volume percent C_3H_6. The absolute value of the deposition temperature of the coatings are not known with certainty, and an estimated error fo ± 50°C is assigned to these values. The relative values of temperature, however, are known to be correct.

3.3.1 Deposition temperature

Fig 4 shows the very strong influence of deposition temperature on the pore spectra. The overall porosity of coatings deposited at a given gas concentration decreases from a deposition temperature of 1100°C, has a distinct minimum at about 1250°C and increases to a nearly constant value between 1600 and 2000°C.

3.3.2 Deposition rate

Despite the weaker influence of the deposition gas concentration compared with the deposition temperature, there is a clear correlation between gas concentration and pore spectra. At deposition temperatures between 12oo and 19oo°C, the concentration of smaller pores decreases and the concentration of the larger pores increases with increasing gas concentration and therefore, if the other deposition parameters are constant, with the deposition rate. As an example, in Fig 5 the pore concentration, related to the 5 Vol-% sample, for pores with 1o, 1oo, and 1ooo Å diameter is drawn as a function of gas concentration. The deposition temperature was 14oo°C. At a deposition temperature of 2ooo°C, the smaller pores as well as the larger pores increase with deposition rate (Fig 6).

3.4 Comparison between irradiation behavior and initial pore spectrum

As mentioned above, the irradiation behavior of a coating is mainly determined by the initial state of the material. Therefore, the initial pore spectra of particles with very different irradiation behavior under identical irradiation conditions have been compared. As a typical result, the pore spectra of a propene coating which exhibited good irradiation behavior and a methane coating which exhibited a poorer radiation resistance are compared in Fig 7. Each comparison of good and poor coatings revealed that the lower the concentration of the 1o - 1oo Å-pores and the higher that of the 1oo - 1ooo Å-pores, the better is the irradiation behavior.

In Fig 8, the change of the 1o, 1oo, and 1ooo Å-pore concentrations of low density propene coating pieces is plotted as a function of the fast fluence. The relative change of the initial pore spectrum, at least up to fluences of $1o^{21}$ n/cm^2, is not greater than 5o %. Therefore, the relatively large differences in the initial pore spectra of different pyrocarbons are changed only insignificantly during irradiation.

3.5 Comparison between pore spectra and density

When the assumption is made that coating consists of pores and solid pyrocarbon, the solid having a mean density ϱ_K, the porosity of the coating can be calculated from the expression $P_\varrho = \frac{\varrho_K - \varrho_M}{\varrho_K}$, where ϱ_M is the measured

sink-float density. In Fig 9 the sink-float density is plotted as a function of deposition temperature and C_3H_6 gas concentration. The porosity of coatings calculated in this manner was compared with the porosity measured by small angle scattering, the comparison being made for 25 different coatings deposited from propene at temperatures between 1250 and 2000°C. The calculations showed that nearly all of the porosity is associated with pores in the size range 10 - 25 Å. In Fig 10, the x-ray microporosity is shown as a function of the sink-float density, the latter ranging from 1.3 to 2.0 gm/cm^3. The mean density of the solid pyrocarbon for all coatings has been calculated to be 2.06 gm/cm^3, but the plot of the data for each deposition temperature indicates that this value is different for each coating and is dependent on the deposition conditions. Therefore, the mean density of the solid pyrocarbon in each sample can be calculated by means of the sink-float density and the x-ray microporosity.

3.6 Influence of the pore spectrum on fracture stress

Fracture stress measurements of 35 different particle coatings showed as strong a correlation with the deposition rate (Fig 11) as did the pore spectra. A dependence between fracture stress and pore spectra was therefore clearly indicated, with $\sigma_z = \exp(-P\sigma)$, where $P\sigma$ is the part of the whole microporosity which contributes to the mechanical behavior. In Fig 12 the fracture stress calculated from porosity measurements is shown as a function of the measured fracture stress. As expected, the larger pores (100 - 500 Å diameter) have the most important influence on fracture stress. For this reason a consistent correlation is not found between density, i.e., pores of about 10 Å, and mechanical behavior since the relative concentration of smaller and larger pores are independent of each other and vary from one set of deposition conditions to another.

3.7 Comparison between microporosity and plasma oxidation results

The higher the concentration of the 100 - 500 Å-pores, and therefore the greater the internal surface area of these pores, the larger the proportion of the material showing a lower resistance to oxidation. This variation in resistance to oxidation is demonstrated by the results of plasma oxidation tests.

4. Interpretation and summary

4.1 Microporosity measurements by small angle scattering are a helpfull tool for characterization of pyrocarbon.

4.2 Deposition temperature as well as the deposition rate, empirically specified today, are quantitatively correlated to the micropore spectrum.

4.3 Comparison between deposition temperature, deposition rate, irradiation experiments, plasma oxidation and pore spectra leads to the same clear results: the lower the overall porosity, the lower the concentration of the pores in the 1o - 1oo Å range and the higher the concentration of the 1oo - 1ooo Å-pores the better is the irradiation behavior of the coating. The change in the pore spectra during irradiation is small compared to the difference in pore spectra observed for individual coatings.

4.4 The density is closely correlated to the 1o to 25 Å-pores, increases with increasing deposition rate in propene coatings at deposition temperatures between 12oo and 19oo°C, but decreases with increasing deposition rate at 11oo and 2ooo°C.

4.5 Fracture stress as well as the resistance of pyrocarbon to oxidation decrease with increasing deposition rate and increasing concentration of the 1oo - 5oo Å-pores.

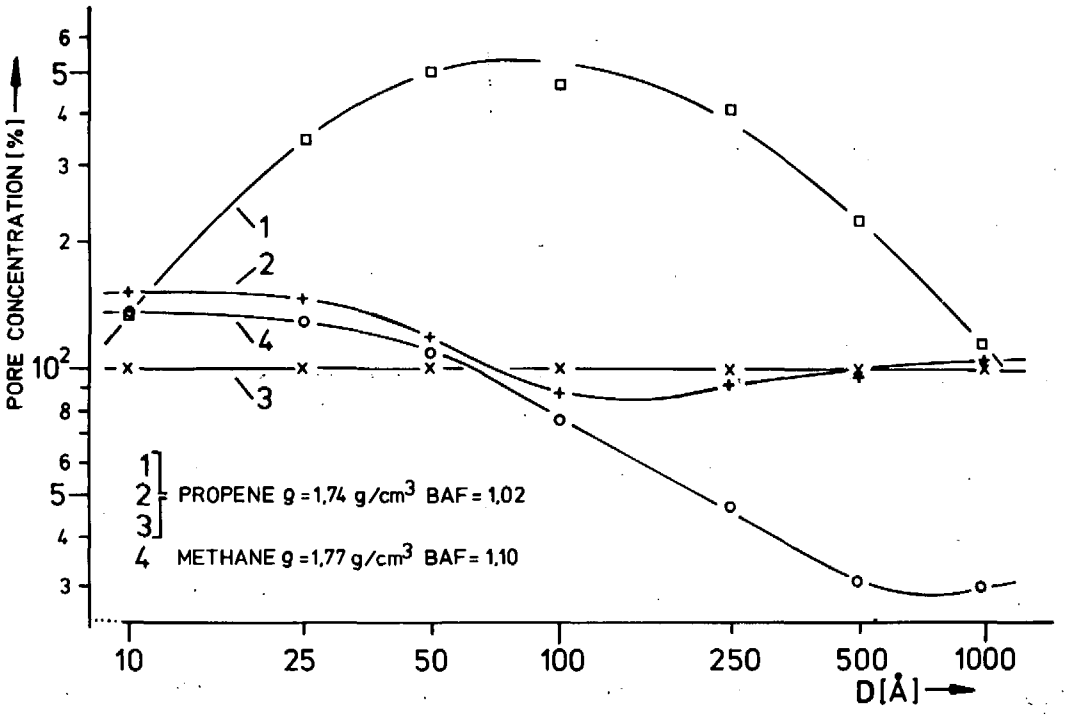

Fig 1 Pore spectra of pyrocarbons with nearly the same density and anisotropy, deposited under different conditions

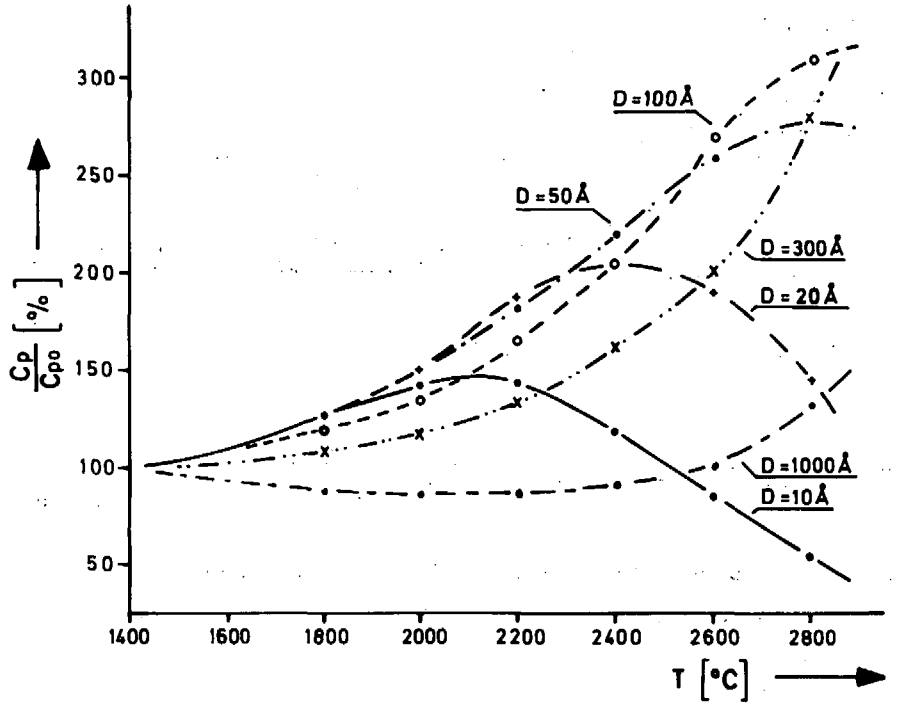

Fig 2 Change of relative pore concentration after heat treatment for 3 hrs at given temperatures

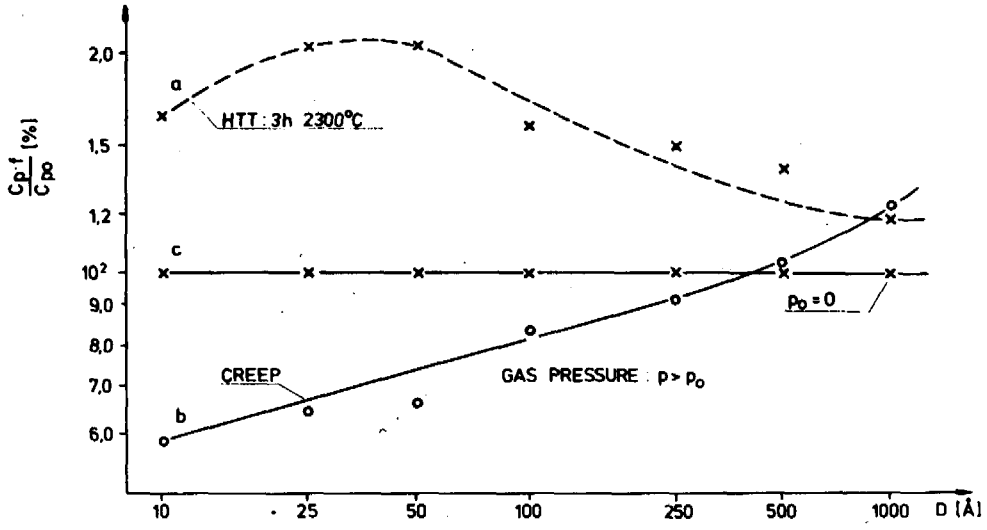

Fig 3 Change of relative pore concentration caused by a: heat treatment, b: creep processes, c: untreated sample

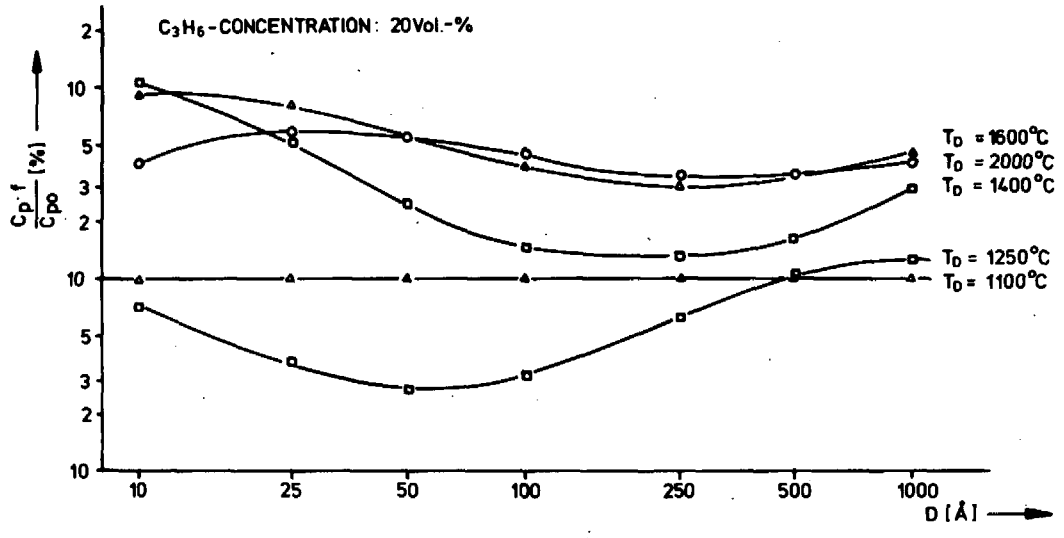

Fig 4 Relative pore concentration for different pore sizes as a function of deposition temperatures

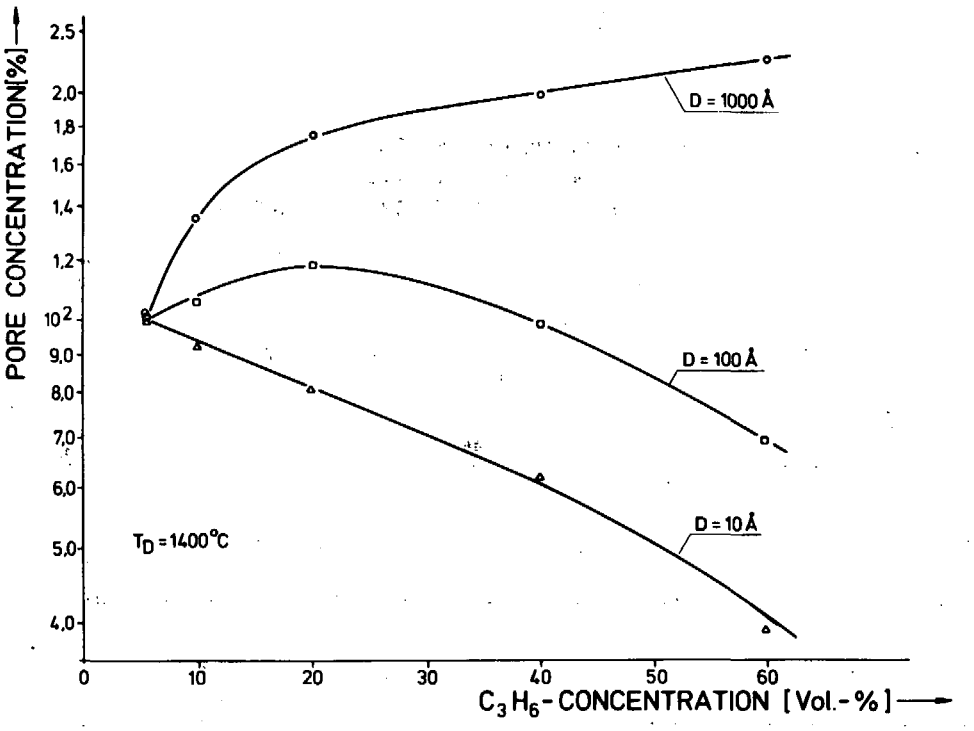

Fig 5 Relative pore concentration as a function of C_3H_6-deposition gas concentration.
Deposition temperature: 1400°C

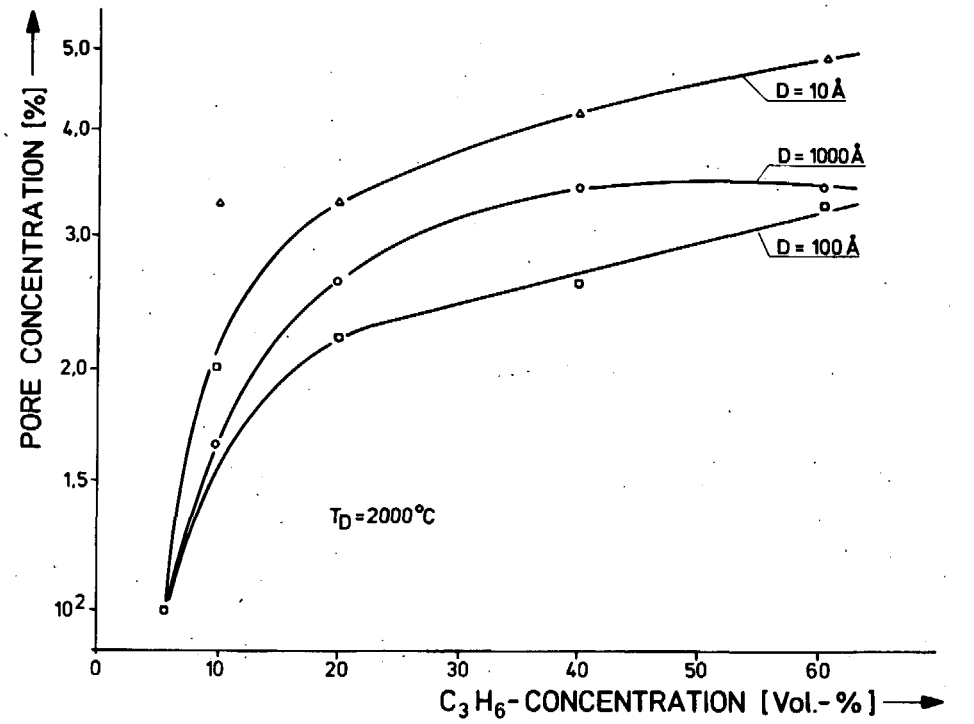

Fig 6 Relative pore concentration as a function of C_3H_6-deposition gas concentration.
Deposition temperature: 2000°C

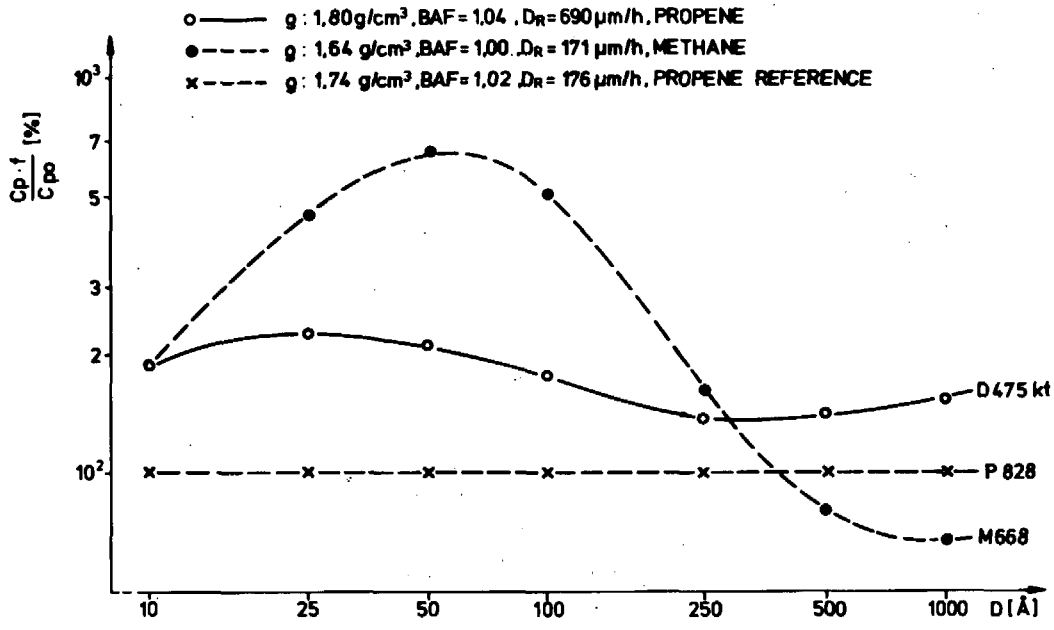

Fig 7 Relative pore concentration of pyrocarbons with different irradiation behavior

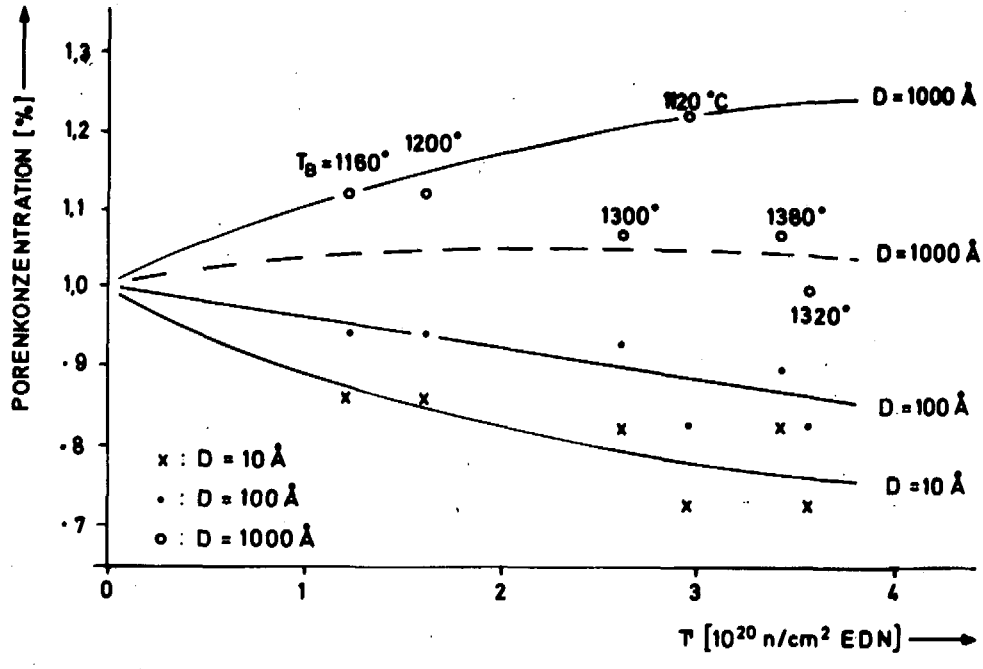

Fig 8 Relative pore concentration of low density propene coating pieces as a function of the fast dose

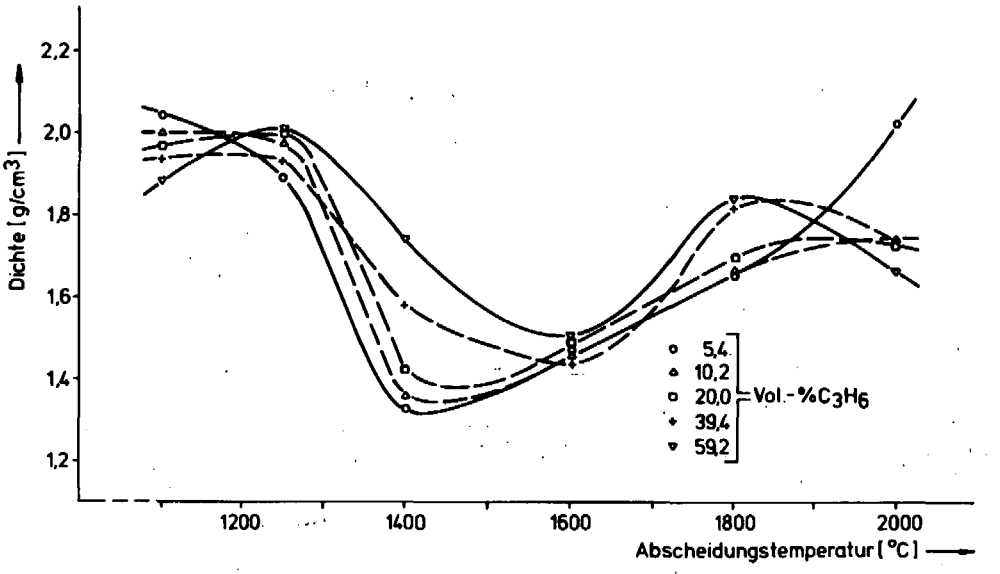

Fig 9 Density of pyrocarbon coatings deposited at different C_3H_6-gas concentrations as a function of deposition temperature

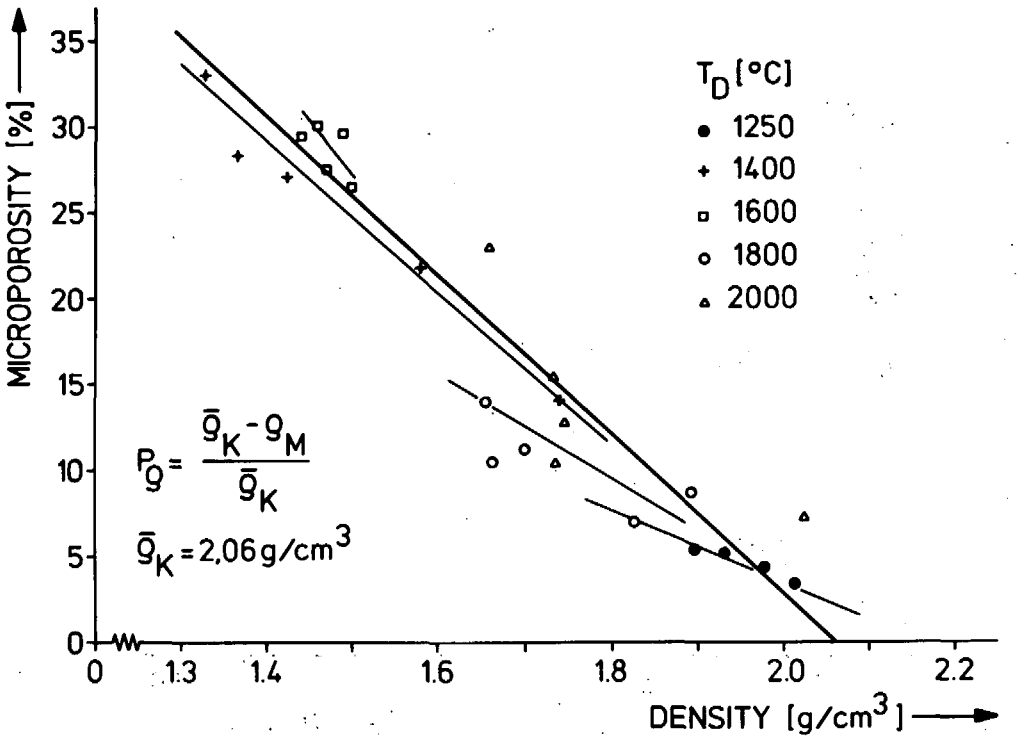

Fig 1o X-ray microporosity of different propene-pyrocarbons versus sink-float density

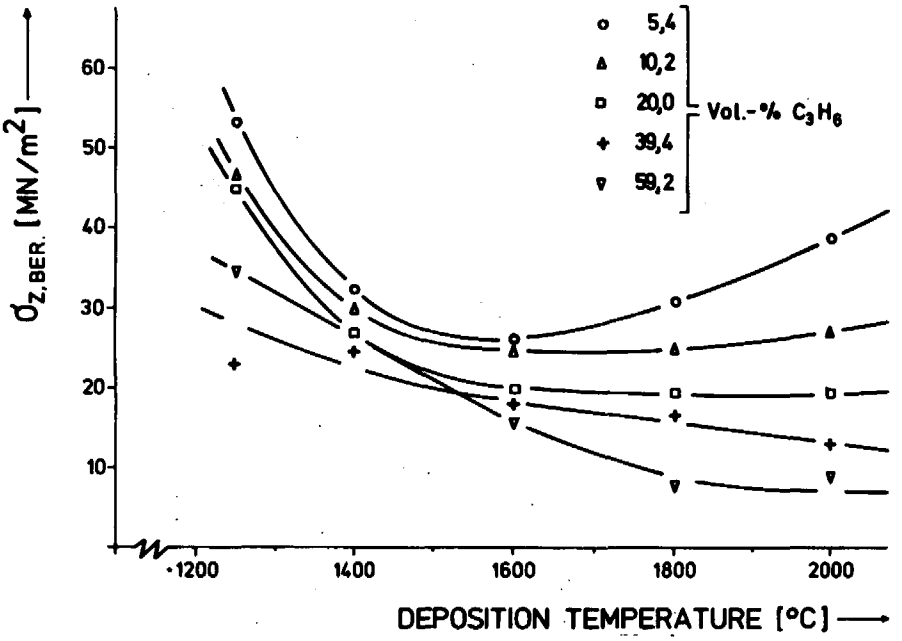

Fig 11 Fracture stress as a function of deposition temperature for different C_3H_6-deposition gas concentrations

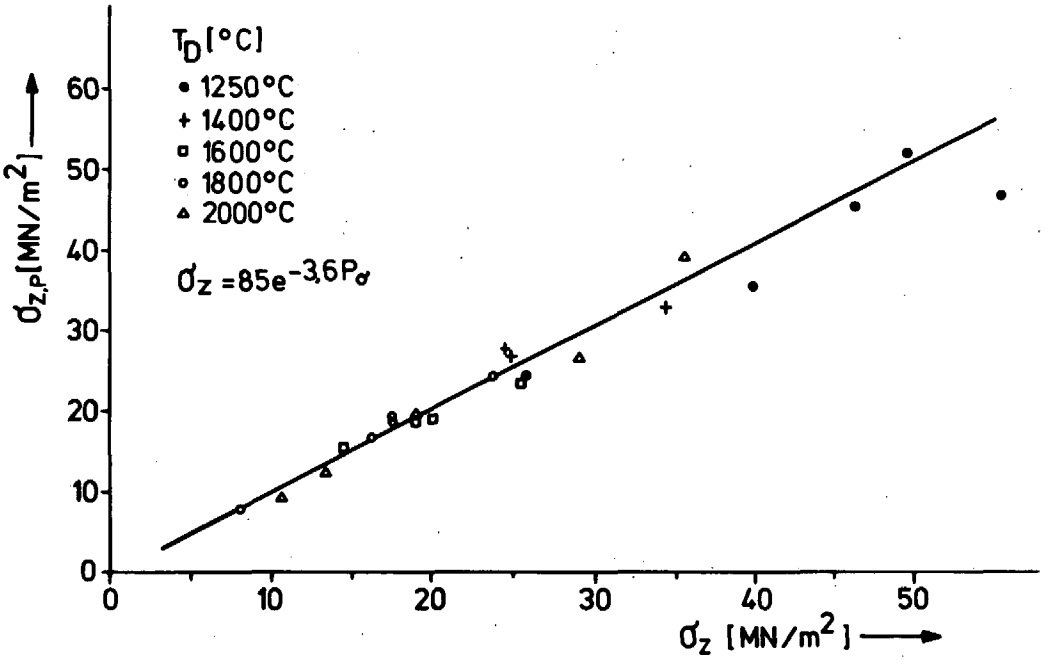

Fig 12 Fracture stress calculated from microporosity measurements versus measured fracture stress

6. Transmission Electron Microscopy of Propene - Derived Pyrolytic Carbon Coatings [+]

by

C.S. Yust [++]

H.P. Krautwasser

[+] Research partially sponsored by the U.S. Atomic Energy Comission under contract with the Union Carbide Corporation

[++] On leave from Metals and Ceramics Division Oak Ridge National Laboratory

1. Introduction

The development and production of pyrocarbon coated fuel spheres with predictable characteristics is of great importance to the field of gas cooled reactor technology. Complete characterization of the coatings produced is necessary to achieve the required understanding of the effect of fabrication process variables, as well as the subsequent service behavior of the coating. Extensive studies at several laboratories in recent years, especially at the Institut für Reaktorwerkstoffe, KFA Jülich, have led to the development of several techniques for the evaluation of specific coating characteristics [1,2,3]. Among the factors evaluated are (1) density, (2) anisotropy, as Bacon Anisotropy Factor (BAF), measured by x-ray or optical methods, (3) distribution of microporosity by small angle x-ray scattering, and (4) coating homogenity, as determined by cold-oxidation techniques. This report discusses the application of yet another characterization method, transmission electron microscopy. This technique has already been applied by Kaae et al. [4], who described structures observed in a variety of pyrocarbon types. The coatings they studied were deposited on flat discs in a fluidized bed, whereas the specimens used in this work are the coatings formed in the fluidized bed on spherical particles. Other characterization measurements have suggested that the coating resulting from deposition on a flat surface is not the same as that deposited on the microspheres [3]. Consequently, it will be of interest to compare the results of this study with that of Kaae et al. where coating conditions are sufficiently similar to permit a comparison.

2. Specimens and Specimen Preparation

The set of specimens used in this work is part of a series of coatings prepared under a controlled range of deposition variables [1]. For a given deposition gas (in this case propene) the temperature is one of the most important deposition parameters, and for this reason we have studied the effect of this variable on coating structure. Deposition rate, however, also influences the microstructure of pyrocarbon, as indicated by irradiation experiments and by microporosity measurements [5], and will also be investigated by transmission electron microscopy in subsequent work.

The deposition temperature of the specimen group varied between 11oo and 2ooo°C, and the gas concentrations used were between 5 and 6o per cent propene in the carrier gas. This entire set of specimens has been carefully characterized by several techniques, and represents a very complete study of the effect of important process variables on the resultant pyrocarbon coating. The work reported here is the first transmission microscope result from these specimens, and presents the structures observed in a series of coatings prepared at temperatures ranging from 125o to 2ooo°C in propene at a concentration of 2o per cent.

The pyrocarbon coatings studied are the outermost coating on the particle which overlays a silicon carbide layer. The coatings were fractured by crushing, and the fractured pieces were then separated from the remaining particle. The pieces of the coating were mixed with a fine aluminium powder and hot pressed at 6oo°C. Thin slices were cut from the resultant compact, which were subsequently ground to about 3o/um in thickness. Small discs containing several coating pieces were then punched from the thinned slice and further thinned to electron transparency by argon-ion bombardment. The argon thinning was performed at approximately 5,5 kV and an ion beam angle of incidence of about 15°. The specimens were examined on a Phillips 3oo electron microscope.

The samples studied and the deposition conditions under which they were prepared are summarized in Table 1.

3. Results

The structures observed in these specimens are presented in Figures 1 through 5, from which it is evident that the structure produced at 1250°C differs markedly from those formed at 1400 - 2000°C. Within this latter group, the structures vary in a specific manner, but contain the same fundamental constituents. Over the entire range of deposition conditions, the coatings are observed to consist of collections of basic structural units, which will be referred to as growth features.

3.1 Structure of the propene coating at 1250°C

The bright field examination of the 1250°C coating reveals a closely stacked array of somewhat polygonal growth features 0.5 to 1.0 μm in diameter, Fig 1a. Cracks can be detected both within and between the growth features, those within the features being circumferentially oriented. The small dark spots seen within each growth feature in Fig 1b are a diffraction contrast effect that may be due to one or more of several effects, including lattice bending. Moiré fringes, or coherent diffraction from small volumes of atoms. In the 1250°C specimen, most of the dark spots are the result of strong diffraction by small volumes of material, which can be thought of as crystallites. This is most clearly seen by reference to Fig 1c, the dark field view of the area shown in Fig 1b, formed by using a portion of the diffracted intensity from the (0002) planes. The position of the (average) diffraction vector, g = (0002), used to form this image of Fig 1c is shown in this figure relative to the image position. Within each bright spot, the (0002) planes are oriented perpendicular to the diffraction vector and essentially perpendicular to the plane of the picture. As the portion of the diffracted intensity selected to form the dark field image is moved around the (0002) diffraction ring, the corresponding region in the growth feature also rotates, and in each instance illuminates volumes of the material within which c-planes are perpendicular to the active diffraction vector. Within each growth feature, then, c-planes are arranged in circular layers, and are primarily in positions nearly perpendicular to the cross-section of the growth feature, i.e., c-planes are tangentially aligned in the

growth feature. Each sector of a growth feature is a region of average orientation within which exist very small volumes of material, approximately 2o - 25 Å in diameter, having a range of separate orientations around the average. Each small volume can be thought of as a crystallite, although true crystallites do not exist in this turbostratic pyrocarbon.

The diffraction pattern obtained from part of a growth feature is shown in Fig 1d. The indexed rings show that the structure is the turbostratic pyrocarbon structure, rather than graphite, containing only well organized c-planes. The incomplete rings reflect the limited orientation range existing in part of a growth feature, and the width of the rings are indicative of the fine crystallite size.

3.2 Structure of the propene coating from 14oo to 2ooo°C

The structures representative of deposition temperatures ranging from 14oo to 2ooo°C are presented in Figs 2 through 5. The fundamental growth features in these coatings are spherical, and approximately o.5 to 1.o µm in diameter. Sharp cracks do not exist between or within these growth features, although regions of lower density which may act as cracks are present between the growth features. Study of these photos reveals that the material can be considered to consist of two components, one of which is an irregular, tangled fiber network containing much fine porosity, the other being regions of layered volumes of varying thickness and extent which often surround the tangled component as an apparent coating, Figs 4a and 5a. The relative amounts of the two components vary in a regular way with the deposition temperature. Clearly, the 14oo°C structure is composed almost completely of the tangled component, Fig 2, while at 2ooo°C, Fig 5, appreciable volumes of the layered component are present. A measure of the change in relative amounts of the two components has been made on a series of random photomicrographs from each structure by means of a point-count technique. The results are presented in Fig 6.

In Fig 2, the center of the growth features are also seen to have a slightly different appearance, as though a nucleus had existed for formation of the tangled component. These central regions appear to

be similar to those observed by Kaae et al. in a low density isotropic carbon deposited from 4o % propane (C_3H_8) at 145o°C, and which they considered to be droplets formed in the gas phase [4].

Bright field and dark field photos of a typical two component region are shown in Fig 4. The coherently diffracting volumes in the outer, layered material are generally large (1oo - 15o Å diameter). As in the case of the 125o°C structure, selection of adjacent portions of the diffracted (0002) intensity results in illumination of neighboring regions of the layered material in dark field. The layered material, therefore, consists of layers of c-planes tangentially arrayed with respect to the spherical growth features. Frequently, separation of sections of layers are observed, forming sharp crack-like openings in the layered material, Fig. 4b.

The central, tangled regions, on the other hand, show a relatively uniform distribution of bright spots in the dark field image for all positions of diffracted intensity used to form this image. The uniform distribution indicates that volumes of pyrocarbon having all orientations are randomly arranged throughout the central region of the growth feature, a result which is consistent with the interpretation of the bright field photos of this material as a tangled network of fibers. Therefore, the 14oo°C specimen, which is composed entirely of of tangled component, does not have a tangentially aligned layer of c-planes at the outer edge of the growth features.

Further support for the description of the tangled regions as networks of fibers is found in the results of high resolution photomicrographs of this material. Fig. 8 is a high resolution photomicrograph of a tangled area in which the lattice planes in a fiber are imaged. Only a short length of the fiber shows the lattice image, since the fiber twists or bends along its length and the appropriate diffraction conditions exist only along a limited length of the fiber. As the plane of focus passes through the specimen foil, short lengths of different fibers show lattice plane images, indicating that parts of fibers exist at various depths in the foil suitably oriented to form

c-plane images. This result is consistent with the conception of the tangled component of the structures as a network-like arrangement of fibers.

Selected area diffraction patterns from each of the two components, Fig. 7, demonstrate the continued existence of the turbostratic pyrocarbon structure, and reveal in the comparison of line widths the relative crystallite size in each component.

The bright field photos, Fig 2a to 5a, of the two component structures reveal numerous dark fringes in the layered component. The fringes are due to diffraction contrast, and are similar to if larger than, the dark spots noted above in the 1250°C structure. In general, the length of the fringes are related to the width of stacks of c-planes, and may therefore be expected to be related to L_c values for the coatings. In the two component coatings, however, the x-ray L_c value is an average for the complete coating and direct comparison of such values with individual fringe lengths is not meaningful. A comparison of the magnitude of change of L_c and fringe length values with variation of deposition temperature shows similar trends in each value.

4. Discussion

The photomicrographs of the 1250°C specimen indicate that this material is relatively dense. This indication is confirmed by the density measurements of the specimens (Table 1) which show the 1250°C specimen to be the most dense of the specimens examined. The density of the tangled component of the 1400 to 2000°C structures would be expected to be relatively low, based on the appearance of bright field, dark field, and high resolution photomicrographs. The density results show that the 1400°C deposition sample, which is composed entirely of tangled component, is indeed the least dense of the specimens. Increasing amounts of the layered, second component in the higher temperature structures correspond to increasing density for these coatings, so that the layered component appears to be of a higher density than the tangled component.

Kaae et al. (4) have also noted the existence of the two components of the microstructure described here as tangled and layered, and reported a variation in size of the tangled region with deposition temperature, although they did not observe a sufficiently wide range of deposition temperatures to note the gradual change in ratio of layered and tangled components. They also interpreted the concurrent change in density as being primarily the result of the appearance of very large (o.5 μm and greater) pores in the structure. A coarse pore structure between growth features is often observed, but pores greater than o.5 μm are generally not evident and are not thought to be an intrinsic part of the structure. Such large openings in the specimen foil are most likely the result of removal of bulk sections of the foil during the final stages of thinning. This effect may be influenced by, and may reflect the presence of, a coarse (o.1 to o.5 μm) porosity component between the growth features which makes selective removal of bulk pieces more probable. In addition, micro-porosity analyses have also shown that even though an increase in larger pores with increasing deposition rate is noted, Fig 9, essentially all of the porosity is associated with pore volumes which are equivalent to spherical pores between 1o and 1ooo Å in diameter (5). The change in density is therefore associated with the change in relative amounts of layered and tangled components in the microstructure, rather than with development of a very coarse pore component.

The specific structure of each of the components of the 14oo - 2ooo°C coatings, however, also varies with deposition temperature. For example, compare the tangled component of Fig 2 with that of Fig 4 or Fig 5 and it is seen that the tangled material formed at 14oo°C is finer than that formed at 18oo or 2ooo°C. The crystallite size parameter, L_c, is also found to be at a minimum at 14oo°C, although this comparison does not directly indicate the relative crystallite sizes between tangled components at 14oo and 2ooo°C. Allowance must be made, therefore, for the possibility of variation of the structure of each of the microstructural components with temperature.

A direct comparison of the results of this study with those of the work by Kaae et al.[4] is not possible since the deposition conditions are not identical for any of the specimens considered. In addition, the deposits on flat discs and spherical fuel kernels are usually not identical, as revealed by crystallite size, cold oxidation, and anisotropy results, as measured at KFA. The conditions are sufficient similar, however, to allow a useful qualitative comparison. In the temperature range of 1300 to 1450°C, using propane (C_3H_8) gas at a concentration of 40 % as compared to propene (C_3H_6) gas at a concentration of 20 % in this work, Kaae at al. observed very similar structures to those reported here [4]. At 1300°C, a tightly packed array of growth features having a very fine crystallite size was observed, while at 1450°C a low density, isotropic structure was reported which appears to be composed entirely of tangled component. These structures are very similar to that observed in this work in coatings prepared at 1250 and 1400°C, especially when the difference in gas, gas concentration and possible deposition temperature inaccuracies are considered. At an intermediate temperature, 1350°C, the structure appears to consist of spherical growth features within which the two components of the microstructure coexist in discrete layers (see Fig 1o of ref. 4). A coating prepared under comparable conditions was not available for this study.

The specimens examined by Kaae in the temperature range 1650 to 2000°C were derived from methane (CH_4), rather than propene, but comparison of the coatings is nevertheless interesting. The 1650°C coating is composed primarily of tangled material, although some layered component is observed. As the deposition temperature is increased, the proportion of layered material increases, as is the case of the propene depositions reported in this work. Density, anisotropy, and average particle size also increase with increasing temperature, consistent with increase in layered material content. Thus, the observations of Kaae et al. are consistent with those of this work.

The porosity distribution in these specimens can be determined by small angle x-ray scattering analysis [5]. The results of such analyses for these specimens are

presented in Fig 1o where the pore distribution is seen to vary distinctly with deposition conditions. Between 125o°C and 14oo°C, as the structure changes from very dense growth features to an apparently highly porous, tangled structure, the relative number of small pores (those less than 25o Å dia.) increases significantly, the greatest increases being in the smallest pore sizes. As the deposition temperature is increased and the proportion of tangled material decreases, the relative amount of the smallest pore size also decreases, and the density increases.

The results of this study may be especially important as a tool for extending the understanding of other pyrocarbon coating characterization methods. For example, the change in microporosity distributions may be more completely understood in terms of the existence and change of the ratio of tangled and layered components, as will be discussed in greater detail in a subsequent paper. The results of oxidation tests on polished pyrocarbon cross-sections may also be more readily interpreted with the knowledge of coating structure which is presented here. The model for the coating structure which has been developed on the basis of cold oxidation tests by Luhleich and co-workers [2] can also be expressed in somewhat greater detail as a consequence of these results. To date, the coatings have been described by the two-component model of Luhleich et al. as consisting of a mixture of a hard, vitreous dense component (HDC), and a carbon-black-like component, (CBC). The oxidation results have been interpreted as delineating the regions of HDC and CBC. The present results show, however, that the layered and tangled components exist on a substantially finer scale than that perceived by means of the oxidation tests. The tangled component, which has an appreciably larger surface area and would be expected to be much more readily oxidized than the layered material, can probably be considered to correspond to the CBC component, while the layered material can be construed as the HDC component. The fine scale on which the layered and tangled material exists, however, suggests that the oxidation tests reveal gradients in the ratio of the two components, rather than discrete regions of either HDC or CBC. These results do not diminish or negate the importance of either the cold oxidation tests or the two component model, but do permit a more thorough understanding of the oxidation results and the coating structure.

It should also be noted that the results presented in Fig 1 through 7 are typical of many observations made on each type of specimen. Variations of structure are noted within each specimen, since the coating structure produced at a particular point in a coating is the result of the specific environmental conditions experienced by the particle at the moment of deposition. The inhomogeneities in deposition conditions within the deposition bed, as well as the uncertainties in the path of the particle through the bed, prevent the formation of perfectly uniform coating structures.

Summary

The study of the microstructure of propene derived pyrocarbon coatings produced between 1250°C and 2000°C at a gas concentration of 20 per cent has shown:

(a) at 1250°C, a dense coating composed of tightly stacked, spherically symmetric growth features having a very fine crystallite size is formed,

(b) the coatings prepared between 1400°C and 2000°C may be composed of two components, one of which is a highly porous tangled network of fibers, the other a dense, relatively ordered, layer-like structure,

(c) the amount of the layered component varies with temperature; at 2000°C the structure is approximately 70 per cent layered, while at 1400°C, the structure is entirely tangled,

(d) the specific nature of each component varies with temperature, the tangled component containing much finer fibers at 1400°C than at 2000°C,

(e) the change in structure observed corresponds to measured changes in density and in pore size distributions.

5. References

(1) Gyarmati, E., Nickel, H.: KFA-Report, Jül-686-RW (1970)

(2) Luhleich, H., Sütterlin, L., Hoven, H., Nickel, H.: Z. Anal. Chem. 255, 97-103 (1971)

(3) Koizlik, K.: KFA-Report, Jül-868-RW (1972)

(4) Kaae, J.L., Gulden, T.D., Liang, S.: Carbon 10, 701 (1972)

(5) Krautwasser, P., Balthesen, E. Nickel, H.: Reaktortagung des Deutschen Atomforums, Berlin, 2.-5.4.1974, Tagungsbericht: ZAED Karlsruhe S. 436-439

Table 1

Spec. No.	Deposition Temperature (1) (°C)	C_3H_6 Gas Concentration (Vol-%)	Average Deposition Rate (µm/h)	Sink-Float Density (g/cm^3)	Apparent Crystallite Size (2) (Å)	BAF (3)	Fracture Stress (4) (MN/m^2)
301	1250	20	230	2,01	40	1,30	47,3
312	1400	20	428	1,43	30	1,04	16,9
317	1600	20	464	1,49	55	1,02	19,0
322	1800	20	470	1,70	80	1,02	17,4
327	2000	20	386	1,73	105	1,04	19,0

(1) The deposition temperatures for all samples were probably approximately 50°C higher than indicated here.

(2) Measured by x-ray diffraction

(3) Measured by optical methods

(4) Measured by crushing the particles

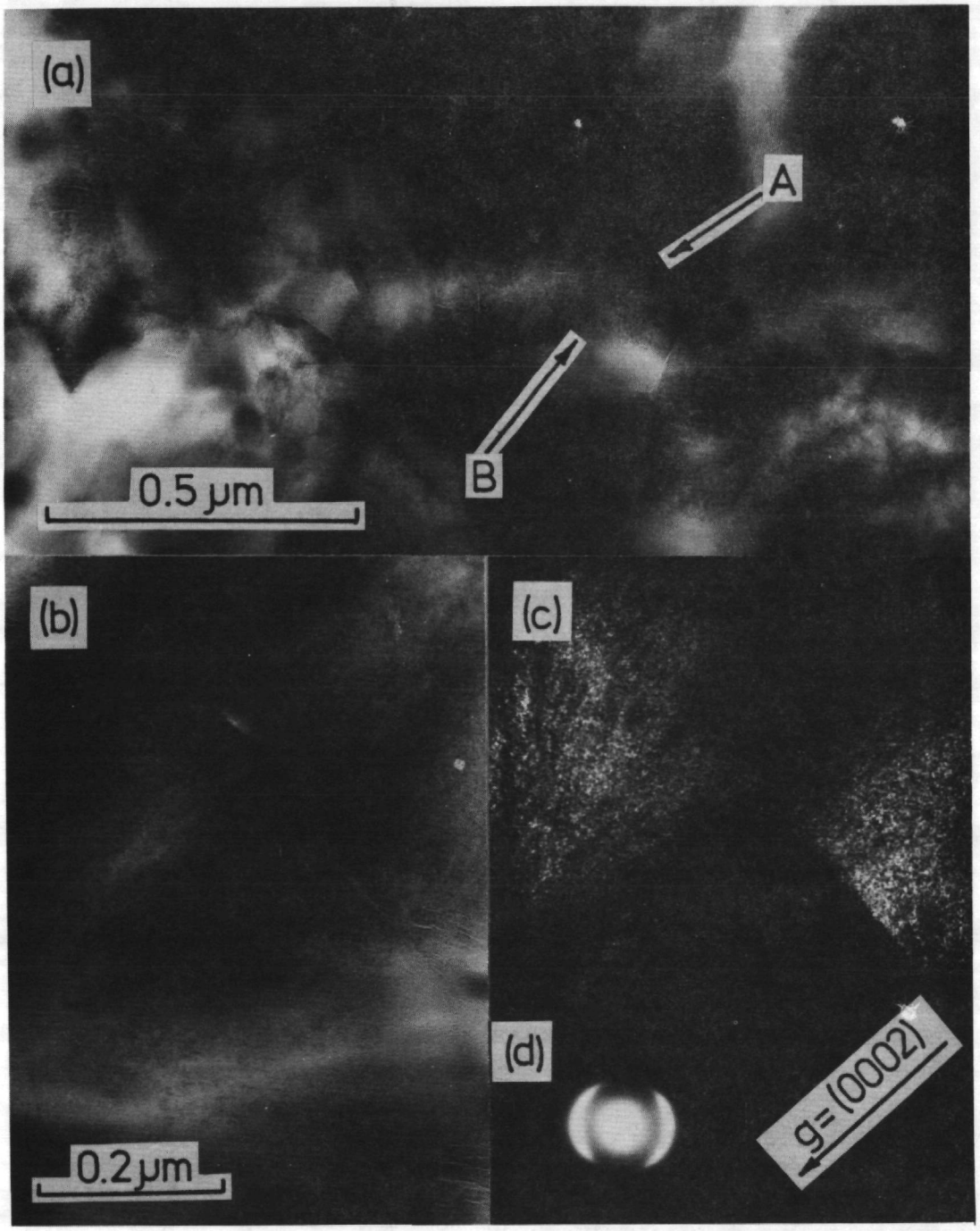

Fig. 1. Coating structure formed from 2o per cent propene at 125o°C. (a) Typical area showing growth features, cracks (A), and diffraction contrast spots (B); (b) higher magnification view of juncture of growth features; (c) dark field view of area of (b) showing diffraction from 'crystallites'; (d) diffraction pattern from part of a growth feature.

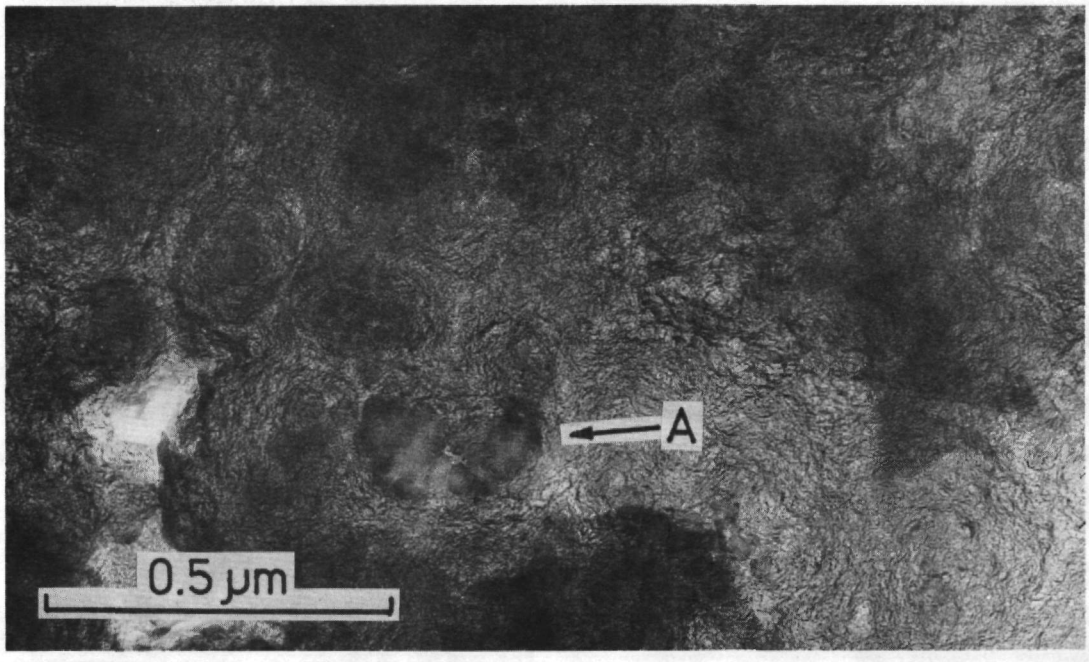

Fig. 2. Coating structure formed from 2o per cent propene at 14oo°C. Feature at (A) is a nucleus-like region observed at center of many growth features. Structure consists entirely of tangled component.

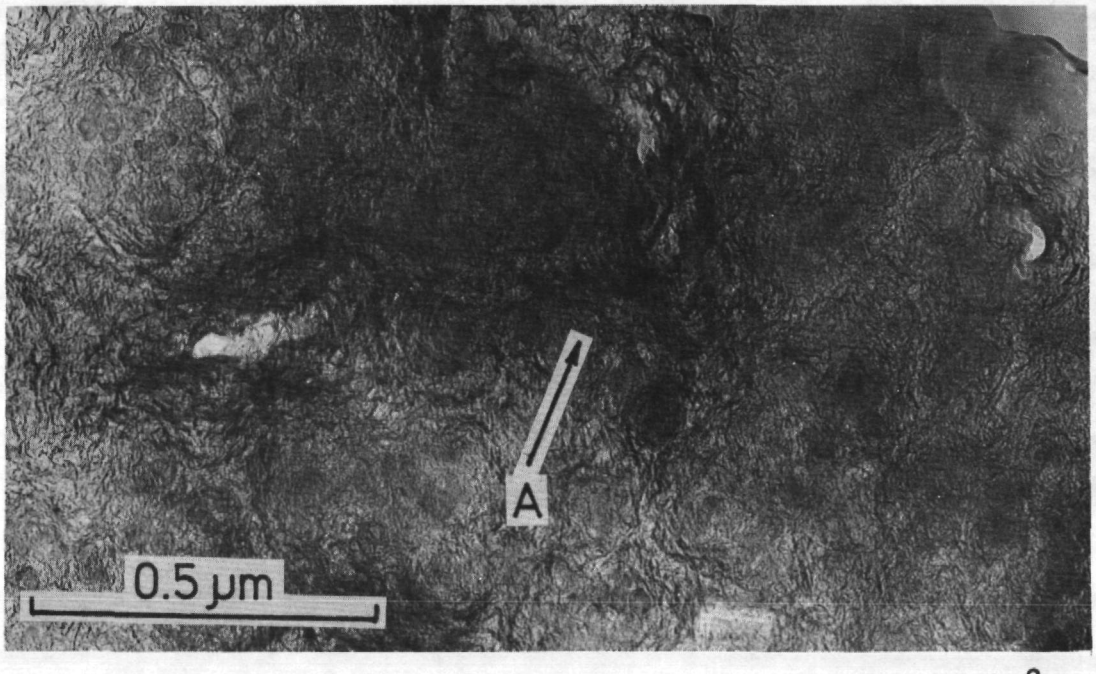

Fig. 3. Coating structure formed from 2o per cent propene at 16oo°C. Structure consists mostly of tangled component, but small amounts of layered material are present, for example at (A).

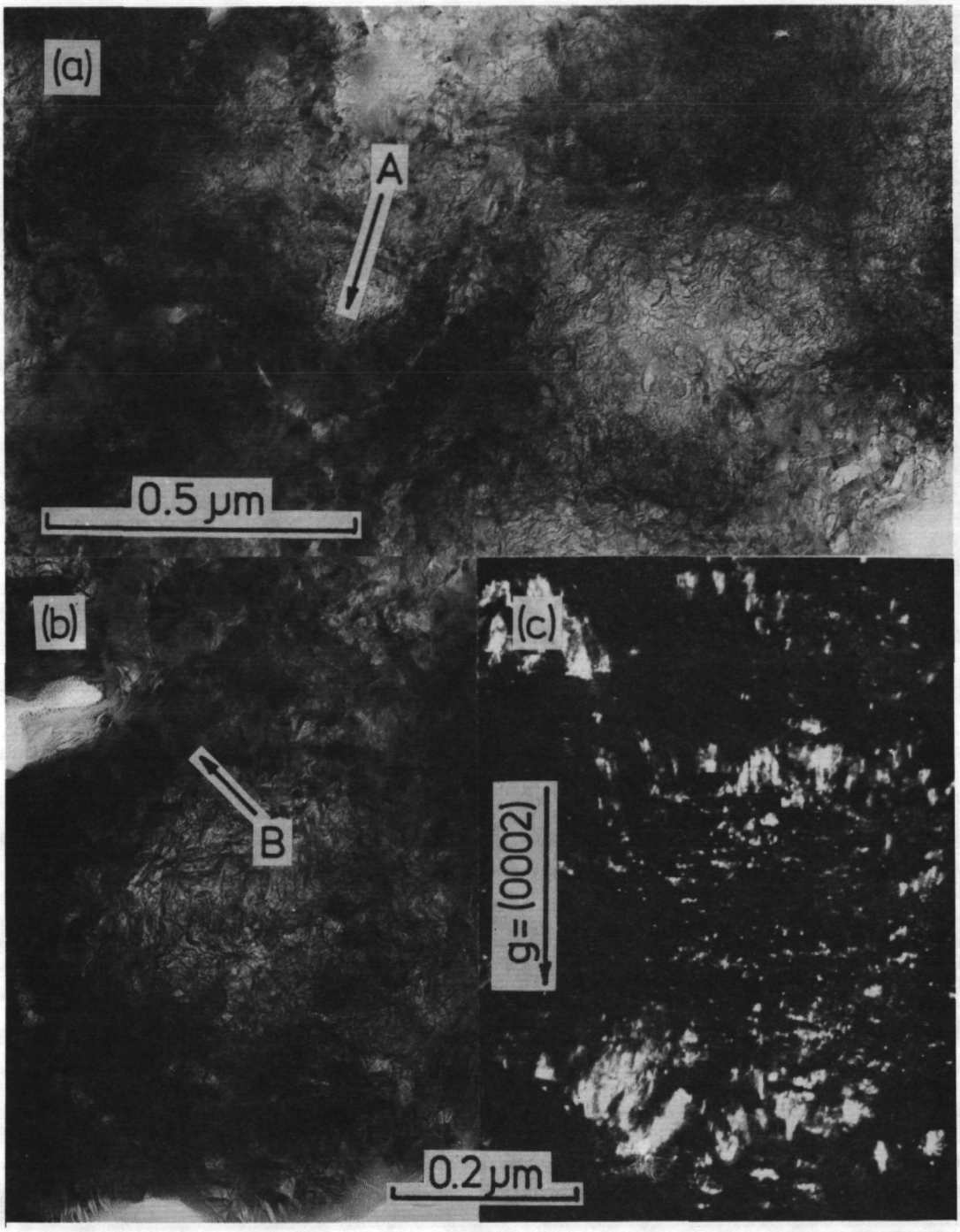

Fig. 4. Coating structure formed from 2o per cent propene at 18oo°C. (a) Structure contains regions of layered material (A) surrounding regions of tangled material; (b) higher magnification view of a typical growth feature, cracks in layered component at (B); (c) dark field view of area of (b) showing difference in 'crystallite' size in layered and tangled components.

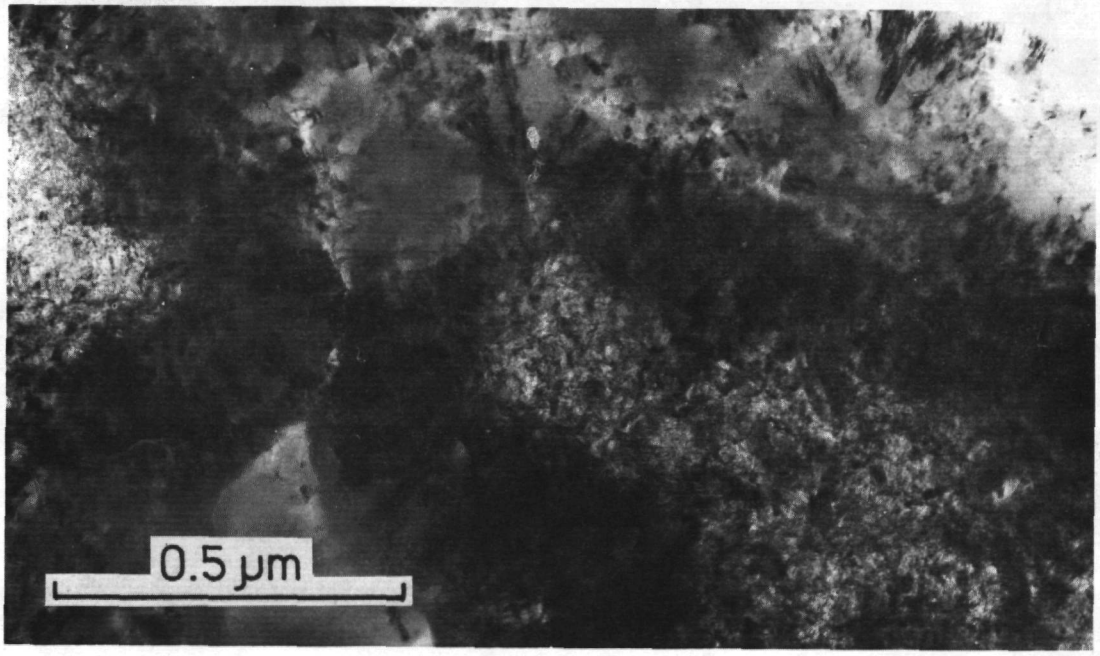

Fig. 5. Coating structure formed from 2o per cent propene at 2ooo°C. Structure contains very large volumes of layered material.

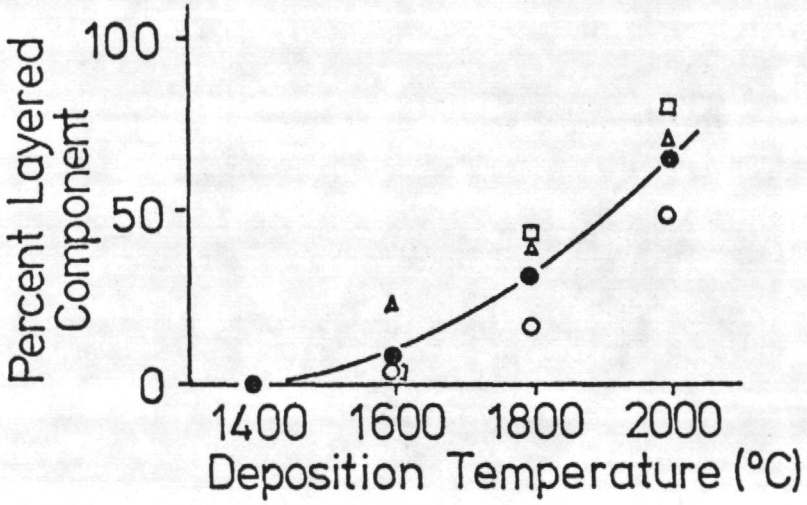

Fig. 6. Fraction of layered component in coating structures formed from 2o per cent propene between 14oo and 2ooo°C. Values shown as solid circles are averaged point count results made on 15 random photomicrographs of each coating by three observers. Individual evaluations by each observer shown as open symbols.

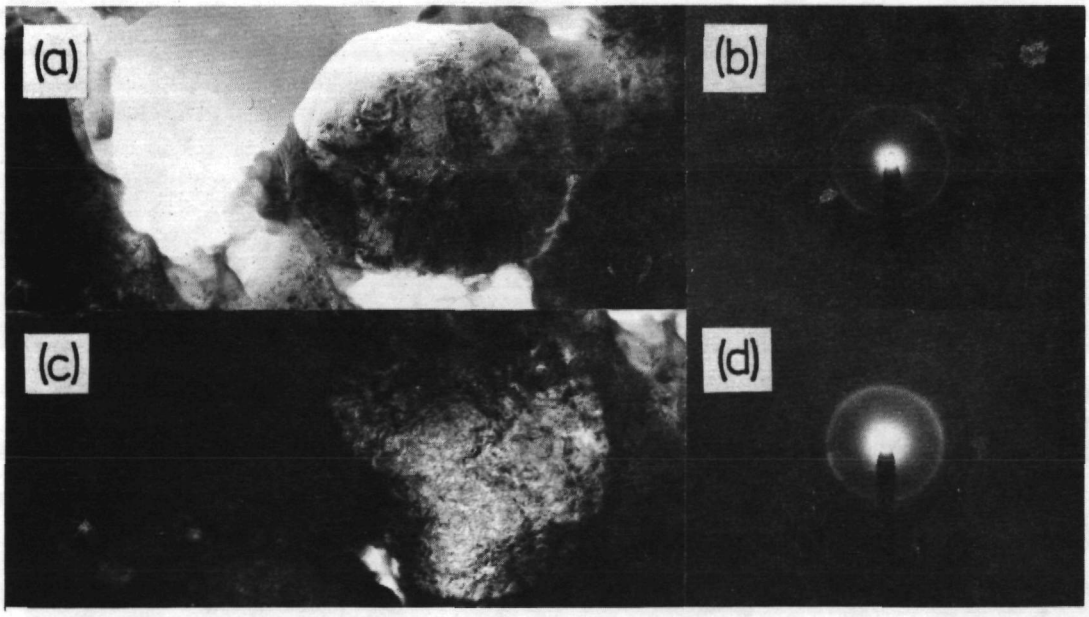

Fig. 7. (a) Selected area consisting largely of layered component yields diffraction pattern (b), while (c) selected area consisting mostly of tangled material yields diffraction pattern (d). The sharper lines seen in (b) reflect the larger effective crystallite size of the layered material.

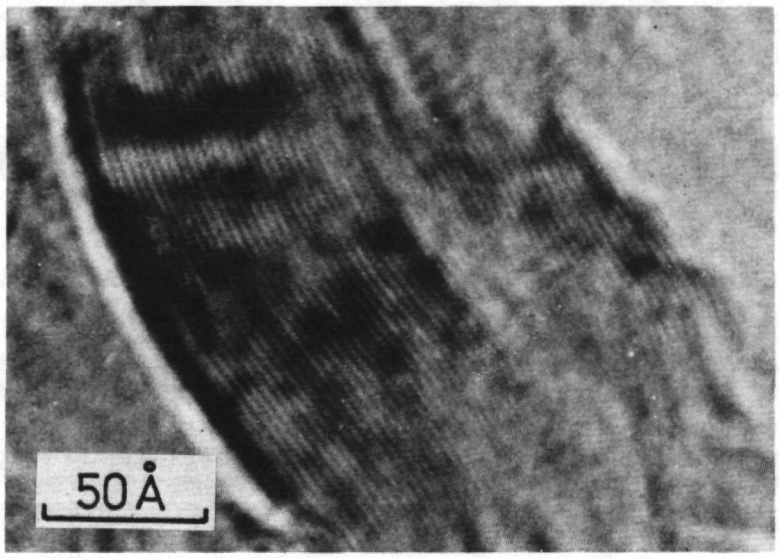

Fig. 8. High resolution photomicrograph of tangled component. Lattice plane images in a single fiber of the tangled network are shown.

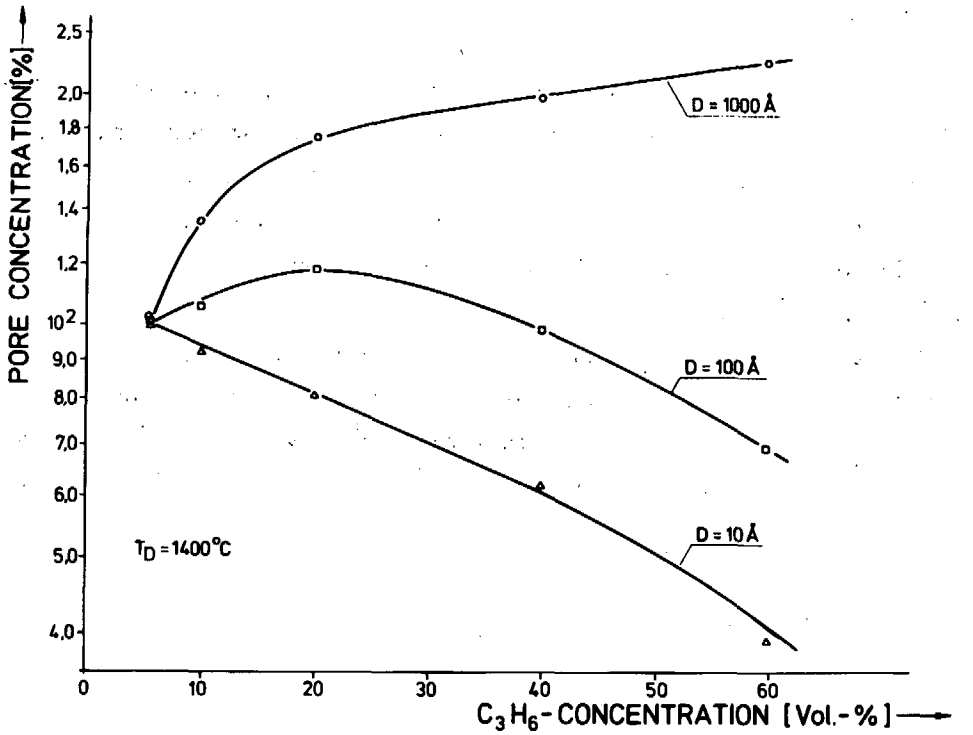

Fig. 9. Relative pore concentration as a function of C_3H_6-deposition gas concentration for coatings deposited at 1400°C. The concentration of each pore size in the reference sample (deposited from 5 Vol-% C_3H_6) is normalized to 100 %.

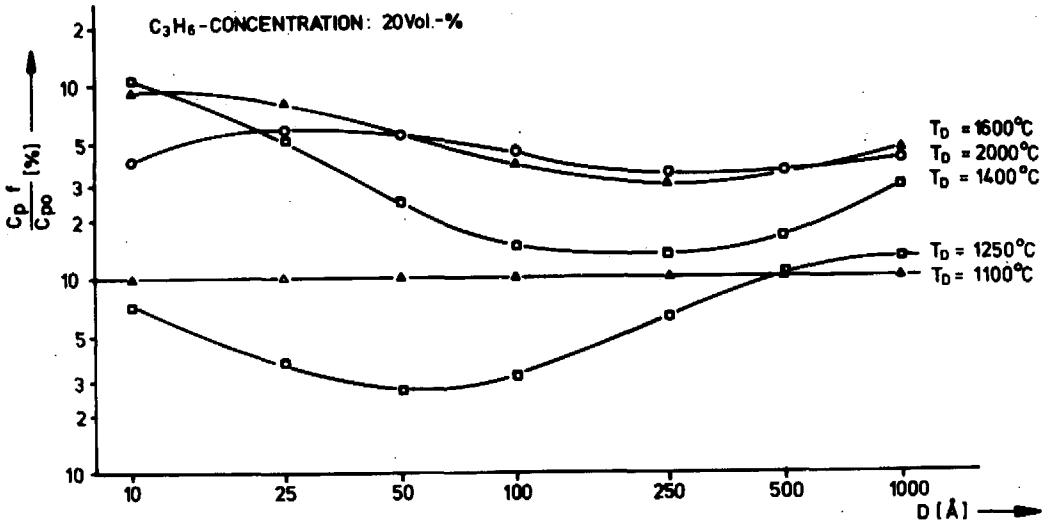

Fig. 10. Relative pore concentration for different pore sizes as a function of deposition temperature. The concentration of each pore size in the reference sample (deposited at 1100°C) is normalized to 100 %.

7. Conclusions

As can be seen by comparing part 2 of this report with part 3, and, with some reservation, the parts 4, 5 and 6, the definition of parameters and the standardization of their measuring procedures of graphite are in an advanced state compared with that of pyrocarbon. So the corresponding work has to be done with very high emphasis to make all necessary informations and procedures available as soon as possible.
To reach that aim, further work and further meetings of the QCWP will be necessary. But as it should be pointed out by the chapters 5 and 6, more basic reserch is also required to reach a satisfactory state of knowledge of the structure and structure changing processes of graphite and pyrocarbon.